Characterization of a Positron Emission Tomography Test Device

Diplomarbeit vorgelegt von Maximilian Schmidt
August 2011

Gutachter
Dr. Erika Garutti
Prof. Dr. Peter Schleper

Institut für Experimentalphysik
Universität Hamburg

Abstract

This thesis is devoted to the characterization of a Positron Emission Tomography (PET) test device featuring Silicon Photomultiplier (SiPM) readout. Measurements as gain, dark rate and time constant of all SiPMs are performed in this work. The results are applied to optimize the voltage working point of the SiPM to equalize the gain or the position of the photoelectric peak in the spectrum for all detector elements. Both methods are discussed and compared concerning energy resolution, number of detected photons and dark rate. The latter method is applied to reconstruct the image of a compound of two ^{22}Na sources in order to determine the spatial resolution of the detector.

Zusammenfassung

Diese Diplomarbeit handelt von der Beschreibung eines Positronen Emissions Tomographie (PET) Testgerätes ausgestattet mit Silizium Photomultipliern (SIPM). Messungen von dem gain, der Dunkelrate und der Zeitkonstante werden in dieser Arbeit durchgeführt. Die Resultate wurden angewandt um die angelegte Spannung am SiPM zu optimieren, so dass der gain oder die position vom photoelektrischen Peak im Spektrum für alle Detektorelemente gleich sind. Beide Methoden werden diskutiert und die Energieauflösung, Anzahl der detektierten Photonen und die Dunkelrate miteinander verglichen. Die letzere Methode wird angewandt, um aus der Bildrekonstruktion zweier ^{22}Na Quellen die Ortsauflösung des Detektors zu bestimmen.

Contents

Introduction

Positron Emission Tomography (PET) is a nuclear medicine imaging technique. A β^+ emitter is used to mark a tracer which is injected into the patient. The emitted positron annihilates with an electron into two $511\,keV$ photons in back-to-back geometry. These photons are then detected by two scintillating crystals read out by two photodetectors . If two $511\,keV$ photons are detected within a certain coincidence time window, their line of response (LOR) is identified. An image of the organ function can be reconstructed from a large set of LOR. In a time-of-flight (TOF) PET device, the time interval of the two photons is measured to narrow down the position of the annihilation point along the LOR.

Important physical parameters of a PET system include: Spatial resolution, energy and time resolution. Spatial resolution describes how well the reconstructed image can be resolved. This depends primarily on the granularity of the detector device which refers to the degree of detail and precision of the detector elements. A good energy resolution is crucial to reject photons which have undergone Compton scattering and hence changed their trajectory. A good time resolution allows to decrease the minimal width of the coincidence time window and, therefore the probability that a coincidence is derived from two photons originated of different annihilations. Both resolutions describe the discrimination of background events in order to reduce blurring of the image. An excellent time resolution is required for the application of the TOF information. This information can be used to reduce noise and improve the image quality of the detector [1].

Nearly all commercial PET scanners are equipped with photomultiplier tubes (PMT). A PMT is based on the multiplication of free electrons produced via the photoelectric effect when a photon hits the photocathode. The Gemini TF PET/CT [2], invented by Philips, is a whole-body scanner which uses Lutetium Yttrium Orthosilicate (LYSO) as scintillating material and PMTs as photodetectors. The device offers a time resolution of about $585\,ps$ and a spatial resolution of $4.8\,mm$. Silicon Photomultipliers (SiPM), also called Multi Pixel Photon Counters (MPPC) when manufactured by Hamamatsu [3], are new photon counting devices made of multiple APD (avalanche photodiode) pixels operated in Geiger mode. They are capable of detecting single photons and have the following advantages over PMTs: Smaller size, insensitivity to magnetic fields and considerably lower bias voltage. Thus, they are very promising devices for application of PET devices.

Small animal PET devices like the DoPET [4] project from the University of Pisa, and the Ax-Pet [5] from the ETH in Zurich, are already using SiPMs coupled to LYSO crystals. They have achieved a spatial resolution below $1.5\,mm$. However, both devices are not suitable for an extension to a TOF PET device since they have the drawback of a high time resolution in the ns range. One of the best time resolution of $220\,ps$ has been achieved for two coincidence channel system [6].

The PET test device used in this work consists of two detector heads containing arrays of $3 \times 3\,mm^2$ MPPCs, each reading out one Lutetium Fine Silicate crystal (LFS) of the same size and of $15\,mm$ length. Inorganic scintillator crystals such as LYSO or LFS are used due

to their high density and atomic number which is crucial to detect $511\,keV$ photons. The performance of LFS as scintillating material is a feature in this thesis since it should provide a similar performance as LYSO with the big advantage of lower cost, which makes it interesting for commercial devices. Measurements with a two coincidence channel system with LFS wrapped in Teflon attached to an MPPC have already reached an energy resolution of 11 % [7]. It has been tested if similar results can be achieved for a multi-channel system. The extension to multi-channels systems requires establishing new readout electronics. In particular allows the test of multi-channel TOF electronics as dedicated chip development for the European project Endo TOFPET-US [8]. This project works on the design of an endoscope probe combining PET with Ultrasound aiming for a time resolution of $200\,ps$ to apply TOF.

The outline of this thesis is as follows: Chapter 1 explains the basic principle of positron emission tomography including time of flight and image reconstruction. The quintessence of PET is the accurate detection of the two back-to-back photons. Accordingly, the detection technology is introduced in chapter 2. The PET test device and its components are then described in chapter 3. The emphasis of this thesis is the characterization of a multi-channel PET test device with MPPC readout. Thus, the most important properties of an MPPC, gain and dark rate, have been measured in chapter 4. The results of the MPPC characterization have been applied to the system determining the MPPC working point in chapter 5. Two readout options have been introduced for different measurements and compared concerning dark rate, energy resolution and number of detected photons. The most suitable system has been applied for image reconstruction of two radioactive sources in chapter 6. The spatial resolution have been determined for various radii of the detector modules. A conclusion and outlook is given in the last chapter.

Chapter 1

Positron Emission Tomography

Positron Emission Tomography delivers a functional image of active regions in a patient. Since cancer cells have a very high metabolic activity, they can be distinguished from healthy tissue. Therefore, PET has proven to be a powerful tool in modern clinical diagnostics. A PET examination starts with the injection of a tracer into the patient (cf. figure 1.1). A tracer is composed of a radioactive positron emitter incorporated into a biological active molecule which is involved in metabolism and hence will concentrate in regions where metabolic activity levels are elevated. A commonly used tracer is fluorodeoxyglucose (FDG), an analogue of glucose. The half-life $\tau_{1/2}$ of the radionuclides should be suited for a patient examination. Typically, they have a short half-life between 2 and 110 minutes (see table 1.1), because this provides a high rate during the examination and a preferably fast disappearance afterwards.

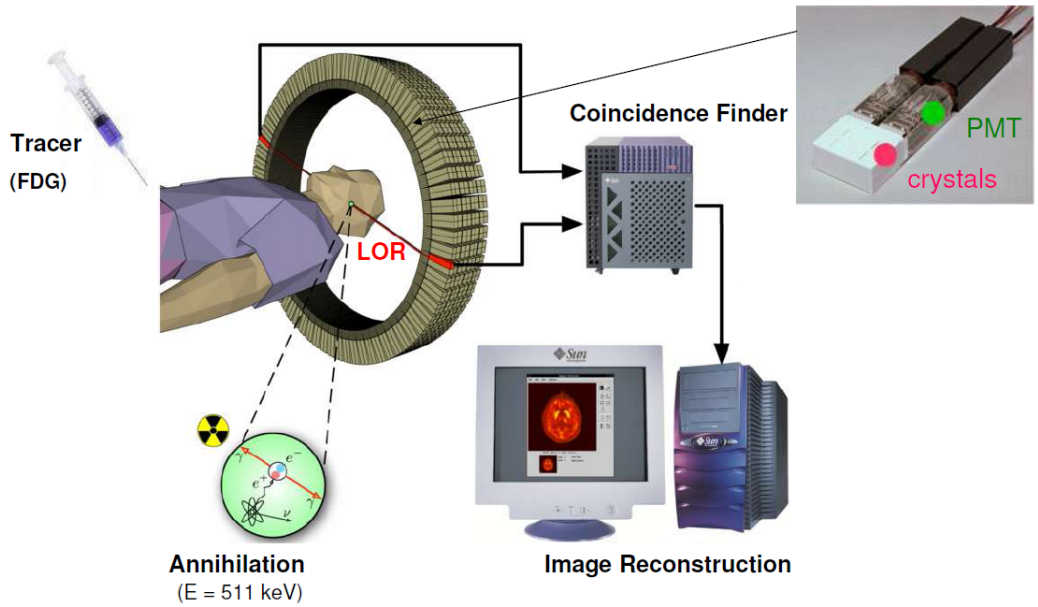

Figure 1.1: Process of a PET examination on a patient. A positron emitting tracer is injected into a patient. The positron annihilates with an electron into two back-to-photons which are detected by crystal coupled read out by a PMT. A coincidence finder determines which photons belong to the same annihilation. A functional image of the tracer is derived from a sufficient amount of coincidences [9].

When a positron is emitted from the nucleus, it has an initial kinetic energy dependent on the radionuclide (see table 1.1). The emitted positron propagates and looses kinetic energy by

ionization and excitation of surrounding atoms until it stops and annihilates with an electron of the surrounding matter (see figure 1.2). The travel distance of the positron is referred to as positron range and depends on the kinetic energy of the positron. The entire mass of the electron-positron pair is converted into two back-to-back $511\,keV$ photons. Because of some residual momentum of the positron at the moment of the annihilation, the angle of the two photons can deviate from 180° up to 0.3°[10]. This effect is referred to as non-collinearity. Together with the positron range, these effects degrade the measured spatial resolution of the detector.

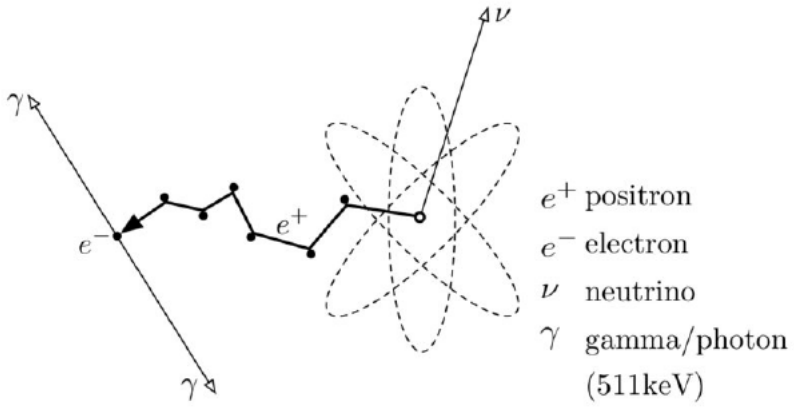

Figure 1.2: β^+decay of radionuclide: A proton decays into a positron, neutrino and neutron. The emitted positron slows down and annihilates with an electron, resulting in two photons of $511\,keV$, each emitted in opposite directions [9].

Photons with an energy of $511\,keV$ mainly interact with matter via photoelectric effect or Compton scattering. When photons interact through the photoelectric effect, they transfer their entire energy to one electron. A photons is diverted from its original track, when it has undergone Compton scattering. In this case, only a fraction of its energy is transfered to the electron.

A Commercial PET scanner usually consist of PMTs coupled to scintillating crystals arranged in a ring-like geometry. If two photons are detected within a certain time window, a coincidence is identified. The circuitry of the scanner then determines the line of response, which is the line in space connecting the locations of the two detector interactions. There are three types of coincidences: True coincidences, scattered and random coincidences (see figure 1.3). They differ in the following way:

- In a true coincidence, both photons are originated from the same annihilation and deposit the full $511\,keV$ into the detector arrays. In this case, the annihilation occurs close to the LOR.

- A scattered coincidence occurs when at least one photon from a single annihilation is scattered, but both are detected. The reconstructed LOR is significantly distant from the origin of the two $511\,keV$ photons.

- In a random coincidence, two photons, originated from different annihilations, reach the detector within the coincidence time window.

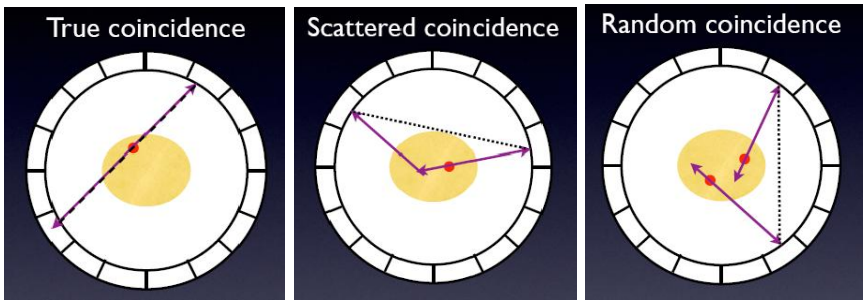

Figure 1.3: Schematics of true (left), scattered (middle) and random (right) coincidences. The arrows describe the photons originated from the annihilation point. The derived LOR is depicted as a dashed line.

The amount of random coincidences can be reduced by setting a smaller coincidence time window. The time resolution describes the sigma of the distribution of the time of arrival difference of two detected photons. Hence, the time resolution has an impact on the minimum width of the coincidence time window. A $511\,keV$ photon which reaches the detector without any interaction, can deposit its whole energy in the detector array. In contrast, when a photon scatters on an electron of the tissue it transfers a fraction of its initial energy and hence changes its trajectory. Because of this, a scattered coincidence can be identified by an energy lower than of photoelectric events. This requires good energy resolution in order to separate the Compton events from the photoelectric peak. Energy and time resolution are important properties because they describe the accuracy of rejecting background events.

Only from a true coincidence, it can be assumed that the annihilation point is located along the LOR. From a large set of such LOR covering a sufficient number of directions, a functional 3D image of the the tracer can be derived.

Radionuclide	$\tau_{1/2}\,[min]$	$E_{max}\,[MeV]$	$R_{mean}[mm]$
^{18}F	109.8	0.63	0.6
^{15}O	2	1.74	2.5
^{13}N	10	1.12	1.5
^{11}C	20.4	0.96	1.1

Table 1.1: Common radionuclides used in PET, together with their half life $\tau_{1/2}$, maximum positron energy E_{max} and mean positron range R_{mean} in water [11].

1.1 Time-of-flight PET

In a conventional PET, the annihilation point is unknown, but expected to lie on the LOR. In TOF PET, the time difference $\triangle\tau$ between the two annihilation photons is measured in order to narrow down the position of the annihilation along the LOR.

τ_1 and τ_2 describe the time each photon takes from the annihilation point to the detector element respectively (see figure 1.4).

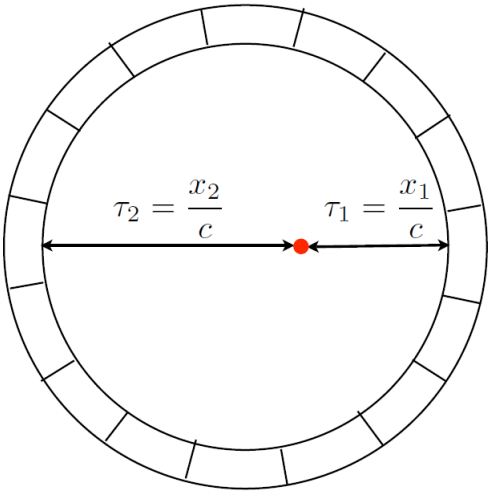

Figure 1.4: Schematic view of a PET detector illustrating the annihilation point and two annihilation photons which travel to the detector elements [12].

The time difference between both photons is

$$\triangle\tau = \tau_2 - \tau_1.$$

From the geometry of the detector the distance d of the detector elements can be determined:

$$d = x_1 + x_2.$$

x_1 , the distance between annihilation point and detector element can be calculated as follows:

$$x_1 = \frac{d - \triangle\tau c}{2}$$

with c being the speed of light. From this equation the position error $\triangle x$ can be derived via error propagation to

$$\triangle x = \frac{c}{2} \triangle t \tag{1.1}$$

where $\triangle t$ is the coincidence time resolution.

A time resolution of $500\,ps$ allows to locate the annihilation point with a precision of$7.5\,cm$ (equation 1.1). Hence, it cannot improve the spatial resolution which achieved results better than $2\,mm$ with conventional methods [4, 5]. Though time-of-flight offers no direct improvement to spatial resolution, it has huge potential for statistical noise reduction. A conventional PET device projects full-length LOR for each coincidence (see figure 1.5). This introduces a significant amount of noise to the resulting image. Applying the TOF information allows to increment a probability for the annihilation on each point of the LOR, which leads to shorter LOR to be projected for each annihilation event. That effectively reduces the amount of statistical noise in the image [13]. The amount of noise decreases with improving time resolution, therefore, TOF PET requires an excellent time resolution.

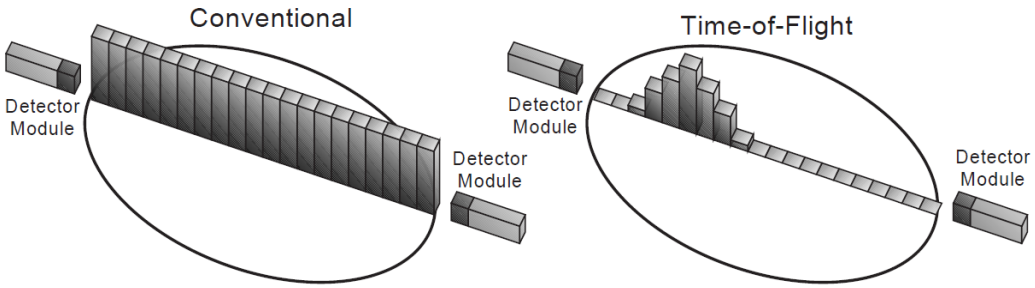

Figure 1.5: For a conventional PET device, every point on the LOR is incremented with the same probability. With a time-of-flight reconstruction, each point is incremented by the probability that the source is located at that position, as determined by the TOF measurement [13].

1.2 Image reconstruction

A functional image in PET is derived from detector systems, placed or rotated around the object in a way that sufficient angular projections of the object are obtained. The coincidence data acquired by these projections are sorted in a sinogram, which is corrected for various distortions and background effects. Mathematical algorithms are applied to reconstruct the image from the sinogram. There are several reconstruction methods to determine the image of a PET scan. This section will focus on the imaging technique filtered backprojection (FBP), which has been used to reconstruct the image in chapter 6.

The detector elements are placed in a ring geometry with radius R around the center. A true coincidence consists of two $511\,keV$ photons detected from opposing detector elements. From both points, a line of response $f(x,y)$ can be derived which makes an angle θ with the y-axis at the smallest distance of approach s to the origin (see figure 1.6 (left)). A new coordinate system (s,u) is defined by rotating (x,y) over the angle θ. This gives the following transformation formulas:

$$\begin{bmatrix} s \\ u \end{bmatrix} = \begin{bmatrix} cos\theta & sin\theta \\ -sin\theta & cos\theta \end{bmatrix} \begin{bmatrix} x \\ y \end{bmatrix} \tag{1.2}$$

$$\begin{bmatrix} x \\ y \end{bmatrix} = \begin{bmatrix} cos\theta & -sin\theta \\ sin\theta & cos\theta \end{bmatrix} \begin{bmatrix} s \\ u \end{bmatrix} \tag{1.3}$$

where u is the distance of both detector elements. The function $g(s,\theta)$ is the projection of $f(x,y)$ on the axis s in θ direction. As depicted in figure 1.6 (left), $g(s,\theta)$ integrates along the line, which normal vector is s in θ direction. The integration of $f(x,y)$ is only satisfied at the points for which $x \cdot cos\theta + y \cdot sin\theta - s = 0$ (see equation 1.2), which is expressed as a δ-function in the following equation:

$$g(s,\theta) = \int \int_{-\infty}^{\infty} f(x,y)\delta(x \cdot cos\theta + y \cdot sin\theta - s)dxdy. \tag{1.4}$$

Equation 1.4 is called radon transform from the 2D distribution $f(x,y)$ to the projection $g(s,\theta)$. Since the projection $g(s,\theta)$ is a line integral, it can be expressed by an integral of one variable. This is performed by the translation of the (x,y)-coordinate to (s,u). In this case, the δ-function depends only on s, which leads to

$$\int_{-\infty}^{\infty} \delta(0)ds = 1.$$

Since the transformation leads to no shrinkage or expansion, $dxdy = duds$ which leads to

$$g(s,\theta) = \int_{-\infty}^{\infty} f(s \cdot cos\theta - u \cdot sin\theta, s \cdot sin\theta + u \cdot cos\theta)du. \tag{1.5}$$

This equation describes the ray sum of all $f(x,y)$ whose smallest distance to the origin in θ direction is s. Displayed as a 2D function this is referred to as the sinogram. Each point in the sinogram corresponds to one LOR of $f(x,y)$. Figure 1.6 (right) shows the sinogram of a single dot.

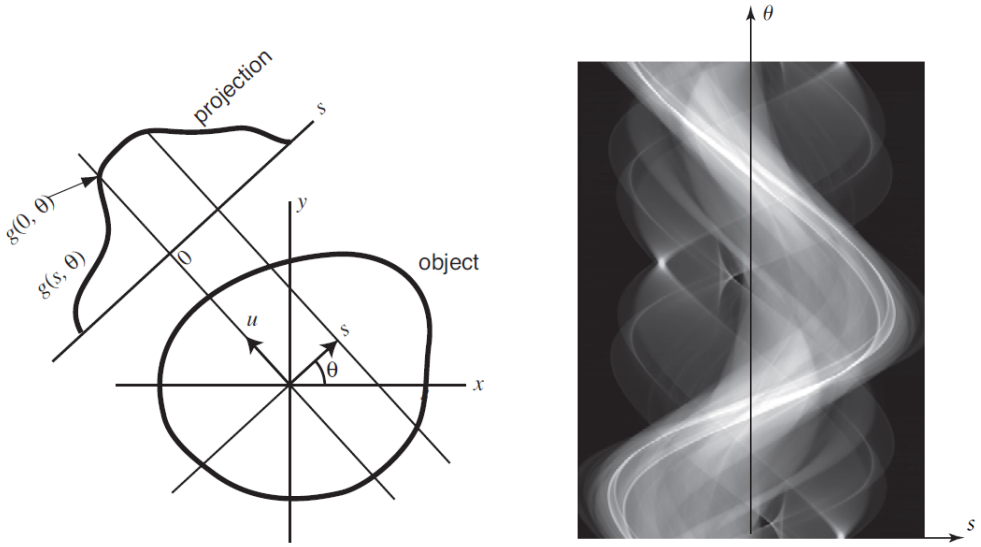

Figure 1.6: Illustration of the radon transform of $f(x,y)$ to the projection $g(s,\theta)$ (left). For one LOR, s is the distance of minimum approach to the center which makes an angle θ with the y-axis (right) [14]. A sinogram is a dataset of all LOR sampled in $g(s,\theta)$. The projection of a distribution containing a single dot into a sinogram has a sinusoidal shape, which explains the origin of the name (right)[10].

Given the sinogram, a convenient way to reconstruct the image is the summation of all projections passing through (x,y) for all θ. Since $g(s,\theta)$ are line integrals through $f(x,y)$, a summation causes duplication of lines and hence blurring of the image. This reconstruction method, called backprojection (BP), leads to the reconstructed image $b(x,y)$. The radon transform of g(s,θ) projected on the axis of angle θ and passing through (x,y) is $g(x \cdot cos\theta + y \cdot sin\theta, \theta)$, where s has been replaced by $x \cdot cos\theta + y \cdot sin\theta$. The summation of $g(x \cdot cos\theta + y \cdot sin\theta, \theta)$ for all θ ranging between 0 and π leads to the following image by the reconstruction method BP:

$$b(x,y) = \int_0^{\pi} g(x \cdot cos\theta + y \cdot sin\theta, \theta)d\theta \tag{1.6}$$

Substituting $g(s,\theta)$ by the expression of the radon transformation in equation 1.4 and rewriting $s = x \cdot cos\theta + y \cdot sin\theta$ 1.6 leads to

$$b(x,y) = \int_0^{\pi} \left[\int \int_{-\infty}^{\infty} f(x',y')\delta(x' \cdot cos\theta + y' \cdot sin\theta - (x \cdot cos\theta + y \cdot sin\theta))dx'dy' \right] d\theta$$

$$= \int \int_{-\infty}^{\infty} f(x',y') \left[\int_0^{\pi} \delta((x'-x) \cdot cos\theta + (y'-y) \cdot sin\theta)d\theta \right] dx'dy'd\theta$$

The application of the following δ-theorem

$$\delta[h(\theta)] = \sum_k \frac{1}{|h'(\theta_k)|}\delta[\theta - \theta_k]$$

and rewriting leads to the following expression of $b(x, y)$:

$$b(x,y) = \int\int_{-\infty}^{\infty} f(x',y') \left[\frac{1}{\sqrt{(x'-x)^2 + (y'-y)^2}}\right] dx'dy'$$

$$= f(x,y) \times \frac{1}{\sqrt{x^2+y^2}} = f(x,y) \times \frac{1}{r} \tag{1.7}$$

where $\times$ represents the process of convolution. Hence, the relationship between the true image and the backprojected image is described by $\frac{1}{r}$ blurring. Although the backprojection theorem can not provided a good reconstructed image it can be extended to a process called filtered backprojection (FBP). An important key to solve this problem is the projection theorem which is illustrated in figure 1.7. It states, that the 1D Fourier transformation of the Radon transformation $g(s, \theta)$ for variable s, denoted $G(\xi)$, is the same as the cross-section of the 2D Fourier transformation of the object $f(x, y)$ measured through the origin in θ direction, denoted $F(f_x, f_y)$:

$$G(\xi) = F(\xi cos\theta, \xi sin\theta) \tag{1.8}$$

where $f_x = \xi cos\theta$ and $f_y = \xi sin\theta$ describe the coordinates, where the plane at θ slices the object f(x,y).

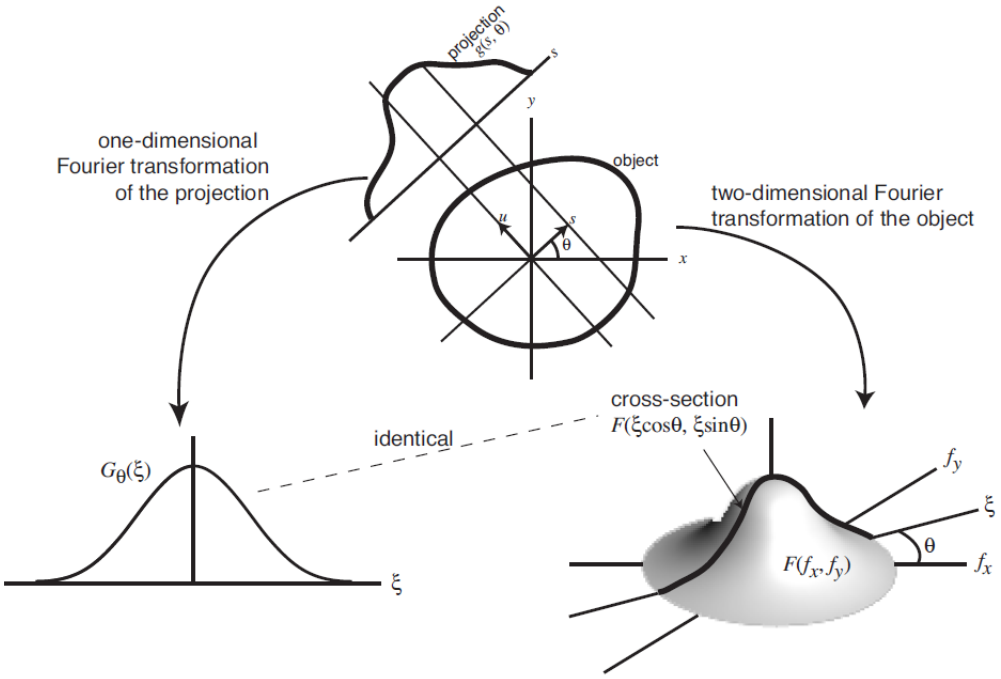

Figure 1.7: Illustration of the projection theorem. The 1D Fourier transform of the the sinogram $g(s, \theta)$ of the object, and the cross-section of the 2D Fourier transform of the object, sliced by the plane at θ perpendicular to the (f_x, f_y) plane, are identical.[14]

Since $f(x,y)$ can be obtained by the inverse 2D $F(f_y, f_x)$,

$$f(x,y) = \int\int_{-\infty}^{\infty} F(f_x, f_y) \cdot e^{i2\pi(f_x x + f_y y)} df_x df_y \tag{1.9}$$

Converting 1.9 into polar coordinates with $df_x df_y = \xi d\xi d\theta$ and using the projection theorem in equation 1.8:

$$f(x,y) = \int_0^{2\pi} \int_0^{\infty} G(\xi) \cdot e^{i2\pi\xi(xcos\theta + ysin\theta)} \xi d\xi d\theta.$$

Rewriting the integration limits of ξ to $(-\infty, \infty)$ and θ to $(0, \pi)$ and employing$s = x \cdot cos\theta + y \cdot sin\theta$:

$$f(x,y) = \int_0^{\pi} \left[\int_{-\infty}^{\infty} |\xi| \, G(\xi) \cdot e^{i2\pi\xi s} d\xi \right] d\theta. \tag{1.10}$$

The equation in between the brackets is the inverse Fourier transform of the function $|\xi| \, G(\xi)$. Defining

$$g'(s,\theta) = \int_{-\infty}^{\infty} |\xi| \, G(\xi) \cdot e^{i2\pi\xi s} d\xi$$

and employing $p'(s,\theta)$ in the inverse polar 2D Fourier transform in equation 1.10, describes the FBP of the image:

$$f(x,y) = \int_0^{\pi} g'(s,\theta) d\theta. \tag{1.11}$$

Comparing the form of this equation to the BP in equation 1.6, states that the original image is obtained by applying the ramp filter $|\xi|$ to the Radon Transform and backprojecting the filtered sinogram, which explains the origin of the name filtered backprojection. The ramp filter amplifies frequencies ξ proportional to their value in the frequency domain (see figure 1.8). Thus with this filter, contrasting features (high-frequencies) are accentuated, while blurring (low-frequencies) is minimized. However, this process has a problem [15]: If the ramp filter amplifies frequencies above the maximum, which are resolvable. The limit ξ_{max} is called "Nyquist frequency". Sampling theory states that the ξ_{max} requires a minimum sampling distance $\triangle r$ given by $\triangle r < \frac{\xi_{max}}{2}$. This means that the highest spatial frequency component to be recovered from the data must be sampled at two points per cycle. Therefore, the ramp filter is cut off at ξ_{max} and the filter function becomes the difference between a rectangular and triangle function.

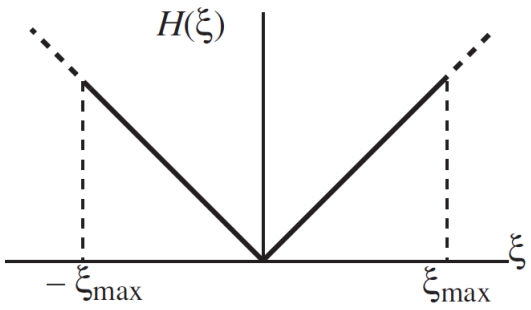

Figure 1.8: For a discrete implementation, the ramp filter $H(\xi)$ is cut off at frequency ξ_{max} [14].

Chapter 2

Detection Technology

The previous chapter was dedicated to the process of deriving an image of a β^+ emitting radionuclide by detecting $511\,keV$ photons originated from the annihilation of positron and electron. In this chapter, emphasis will be given on the technology to detect these photons. For this purpose, inorganic scintillators are coupled to photodetectors such as APDs, PMTs or SiPMs. The scintillating crystal convert the $511\,keV$ photons into a burst of optical photons which are detected by photodetectors. This chapter explains the working principle and physics of detecting $511\,keV$ photons with inorganic scintillators and the scintillation light using semiconductor detectors.

2.1 Detecting 511 keV photons using inorganic scintillators

Inorganic scintillators are a class of scintillating materials with high densities compared to organic plastic scintillators around $4 - 8\,g/cm^3$ [16]. Due to their high density and atomic number, they are used in applications where high conversion efficiencies for photons are required. Due to this properties crystals have a high light yield and therefore provide an excellent energy resolution down to energies of a few hundred keV. The light yield is the number of emitted optical photons produced per energy under gamma or X-ray irradiation and is one of the most important properties of a crystal [17]. The first step of the detection of a $511\,keV$ photon is the interaction with the crystal material leading to the ionization of an atom. The emitted electron ionize and excite other electrons which starts the scintillation process.

2.1.1 Interaction of photons with matter

Photons with an energy below $1\,MeV$ mainly interact via photoelectric effect or Compton scattering:

- Photoelectric effect: A photon with E_γ is absorbed by an atom while its energy is completely transferred to an electron. Due to momentum conversation the electron escapes from the atom in the direction of the incoming photon. The kinetic energy of the electron is

  $$E_e = E_\gamma - B$$

  where B is the shell binding energy, the minimum energy to ionize the respective atom. The probability for photoelectric absorption increases for atoms with high atomic number Z and low energetic gammas by

  $$p \approx \frac{Z^4}{E_\gamma^3}$$

The photoelectric absorption dominates in human tissue at energies below 100 keV. Thus it has little impact for the 511 keV photons resulting from the positron-electron annihilation until it reaches the detector elements. For this reason the inorganic scintillators are chosen with high Z.

- Compton effect: A photon with an energy E_γ transfers a part of its energy to an electron which recoils and is ejected from its atom. The energy E'_γ of the deflected photon can be expressed as:

$$E'_\gamma = 1 + \frac{E_\gamma}{m_e c^2} \cdot (1 - cos\theta)$$

with c being the speed of light and m_e, the mass of the electron. The higher the transferred energy the larger the deviation angle θ of the scattered photons up to 180°, where the minimum value of E'_γ is reached.

2.1.2 Scintillation process

The scintillation process occurs with the deposit of energy in the crystal. The incident 511 keV photon ionizes a crystal atom by photoelectric effect or Compton scattering. The emitted electron ionizes and excites other atoms, which leads to a burst of optical light in the de-excitation process.

Scintillators can be described by the energy band structure (see figure 2.1). When a charged particle passes the crystal, an electron is excited from the valence band to the conduction band. Without activator states, the electron would subsequently fall back to the ground state under emission of a photon offering the same energy needed for further excitation. If activator states are present the excited electron performs a fast non-radiative transition from the conduction band to one of the activator states. Photons performing a radiative transition from the activator states to the states slightly above the valence band do not have the energy to excite electrons from the ground state and can pass the crystal without being absorbed.

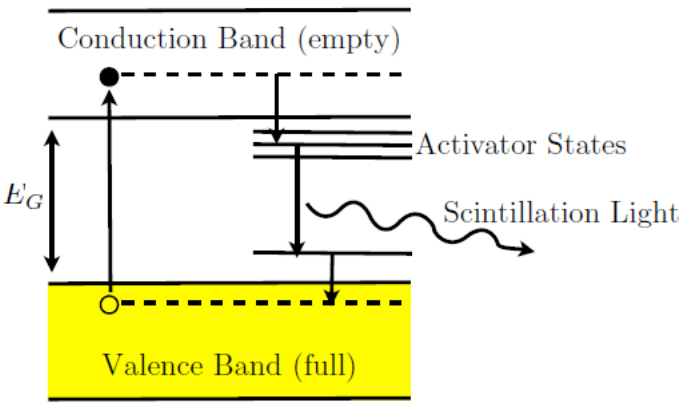

Figure 2.1: Illustration of the energy band model for a scintillator [12].

2.1.3 Intrinsic energy resolution

The energy resolution of the photoelectric peak describes how good photoelectric events can be separated from Compton events. The energy resolution (see section 5.2) depends on the light yield and intrinsic energy resolution of the crystal which depends primarily on two causes:

- Non-linearities: The light yield depends on the energy of the incident photon. If the light yield is not linear to the amount of deposited energy, this is called non-linearity. For some scintillators like LSO this effect occurs for energies below $200 - 300\,keV$ [18].

- Inhomogeneities and impurities: Every crystal has impurities and inhomogeneities. The crystal structure is composed of atoms or molecules arranged in a periodic lattice. Deviations from this structure are called inhomogeneities. In the case of an impurity, a different kind of atom is incorporated at a regular atomic site in the crystal structure. When an incident photon interacts with the crystal at a position which contains inhomogeneities or impurities, the crystal will give different response in form of scintillation light.

2.2 Detecting light with semiconductors

In the previous section $511\,keV$ photons have been converted into optical light by the scintillation process in the crystal. These optical photons have an energy of a few eV and can be detected by photodetectors. This section will explain the fundamentals of semiconductors and detail the working principle of a new type of semiconductor detector, the SiPM.

2.2.1 Semiconductor and p-n junction

A semiconductor material is generally a crystalline solid which structure can be described by the energy band structure (see figure 2.2). At low temperatures, the energy gap is large. Because of this, most of the electrons are bound in the valence band and the conduction band is almost empty. At higher temperatures, the thermal energy $E_{th} = k_b \cdot T$ increases, and hence, the probability for electron excitation into the conduction band. In this process, an electron is produced in the conduction band and a hole in the valence band, referred to as electron-hole pair.

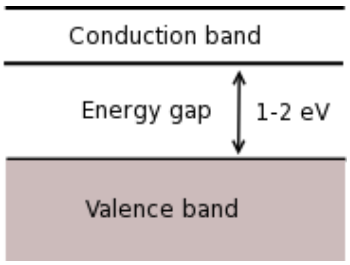

Figure 2.2: Schematic view of the energy band structure of a semiconductor material. Typically the band gap is between 1 and $2\,eV$. The band gap of silicon is $1.14\,eV$.

A photon with sufficiently high energy transfers its energy to an electron by Thompson scattering or Photoelectric absorption and lift it from the valence band to the conduction band. If the photon energy is lower than the band gap, the generation of an electron-hole pair is possible, if an intermediate state is available. Lattice impurities can cause an intermediate but they can also be added intentionally in a process called doping to modulate the electrical properties of the lattice (see figure 2.3). The semiconductor material silicon has four covalent bonds. By adding an atom with five covalent bonds, one electron is only weakly bound and can easily be excited. This introduces a new donor state close to the conduction band. Such a material is referred to as n-doped. The opposite is the case by adding an atom with three valence electrons. These new acceptor state can trap an electrons, which generates a free hole and is located slightly higher than the valence band. This is called p-type doping.

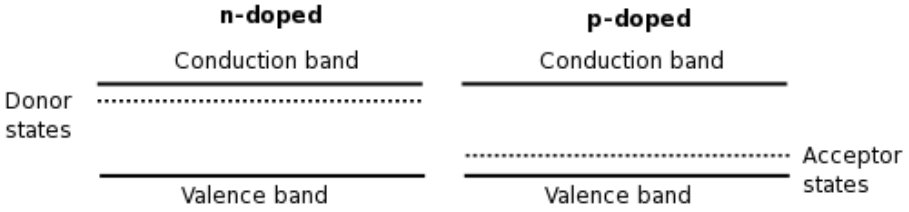

Figure 2.3: Schematic view of the energy band structure in the case of n-doped and p-doped semiconductors.

A junction of p-doped and n-doped semiconductors (see figure 2.4) leads to a diffusion current of the electron to the p-side and the holes to the n-side where they combine. This process generates a depletion region, which is a thin layer at the interface of the p-n junction where almost no free charge carriers remained. An electrical field is generated due to the increased negative charge in the p-region and positive charge in the n-region. Equilibrium is reached when this electrical field compensates the diffusion process. If an electron-hole pair is produced by photon absorption in the depletion region, the electric field causes the electron and the hole to rapidly drift towards the cathode and anode respectively. Consequently a current proportional to the photon flux is generated. If an electron-hole pair is produced outside the depletion region, it is more likely to recombine before reaching the high field region. Hence, the detection efficiency outside the depletion region is reduced.

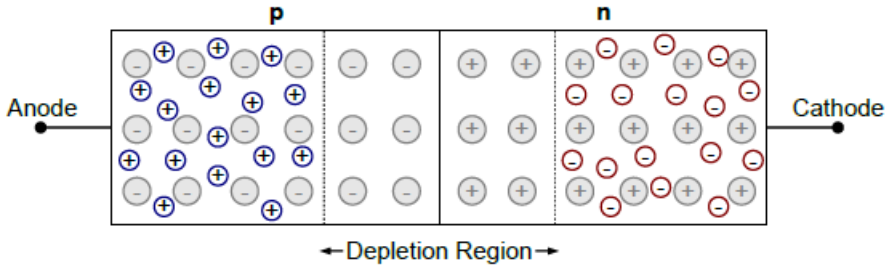

Figure 2.4: Schematic view of a p-n junction. Electrons near the interface tend to diffuse to the p-region and holes to the n-region where they combine respectively. This process generates a depletion region near the interface. An electrical field is generated due to the increased negative charge in the p-region and positive charge in the n-region, which opposes the diffusion process.

However, the width of the depletion region can be increased by applying a reverse bias voltage on the p-n diode. The depletion region exhibits a capacitance C_D which decreases with increasing width d of the depletion region:

$$C_D = \frac{\epsilon_r \epsilon_0 A}{d} \tag{2.1}$$

where A is the diode surface,ϵ_r the dielectric constant and ϵ_0 the permittivity in vacuum. The capacitance decreases with increasing bias voltage until its minimum value is reached. This is the case, when the depletion region is extended to the total volume of the semiconductor material.

The width of the depletion region also determines the spectral sensitivity of the diode since the absorption depth of the photons depends on their wavelength. The absorption probability is assumed to be constant throughout the material. If n photons of a wavelength λ hit the surface of the diode, the probability to absorb the fraction of dn photons at a distance dx in

the material can be described as $dn/n = \mu dx$. The number of photons n of wavelength λ at the depth x can be calculated to

$$n = (1 - R) \cdot n_0 \cdot e^{-\mu(\lambda)x}$$

where n_0 is the initial number of photons, $\mu(\lambda)$ the absorption coefficient depending on the wavelength λ and R describes the reflection probability of photons on the surface. Figure 2.5 shows the absorption coefficient as a function of the wavelength for various materials. It is most sensitive to photons in the ultra-violet and blue light blue region region and decreases for longer wavelength. In particular blue light around $\lambda = 400\,nm$ will only penetrate roughly one micrometer in the material due to the high attenuation coefficient. In order to achieve a good detection efficiency, the photons should not be absorbed before reaching the depletion layer. The emission spectrum of inorganic scintillator materials usually have a maximum in the blue and ultraviolet region. Hence, the covering layers should be very thin around one micrometers in order to detect the scintillation light. By adding an intrinsic layer between the p- and n-layer the detection efficiency can increase, especially for longer wavelengths. Such a device is called PIN-photodiode. When the device is used under moderate reverse bias voltage, the depletion region extends over the complete intrinsic layer resulting in a higher detection efficiency. Hence, the diode capacitance also reduces (see equation 2.1). Since the width of the depletion layer is basically determined by the width of the intrinsic layer the detection efficiency is stable under fluctuations of the bias voltage once the intrinsic layer is depleted completely. PIN- and pn-photodiodes have no intrinsic charge amplification, which results in a stable response concerning temperature fluctuations. However, photodiodes cannot detect single photons due to the missing gain. The gain is the amount of charge carriers generated from an incident photon and will be explained in more detail in the next subsection.

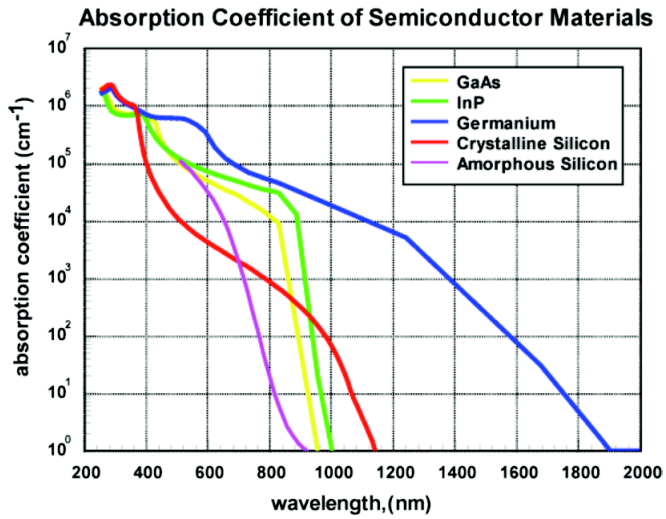

Figure 2.5: Absorption coefficient for different semiconductor materials as a function of the wavelength between 200 and 2000 nm [19].

2.2.2 Avalanche photodiode

An APD is similar to a diode since it is essentially a p-n junction. The main difference is that the APD is operated at a high reverse bias voltage of typically $10^2\,V$ to $10^3\,V$, which results in a large depletion region and high electrical field at the p-n junction. Due to the high electrical field, electron-hole pairs can gain enough energy between two interactions to produce a secondary electron-hole pair. This process is referred to as impact ionization and

leads to a multiplication of electron-hole pairs. An important parameter thereby is the impact ionization coefficient α, which is the number of electron and hole multiplication per cm. α increases exponentially with increasing field (see figure 2.6), but decreases with increasing band gap. The impact ionization coefficient is generally different for electrons and holes. In case of silicon this results in two different operation modes depending on the applied bias voltage: The linear mode and Geiger mode.

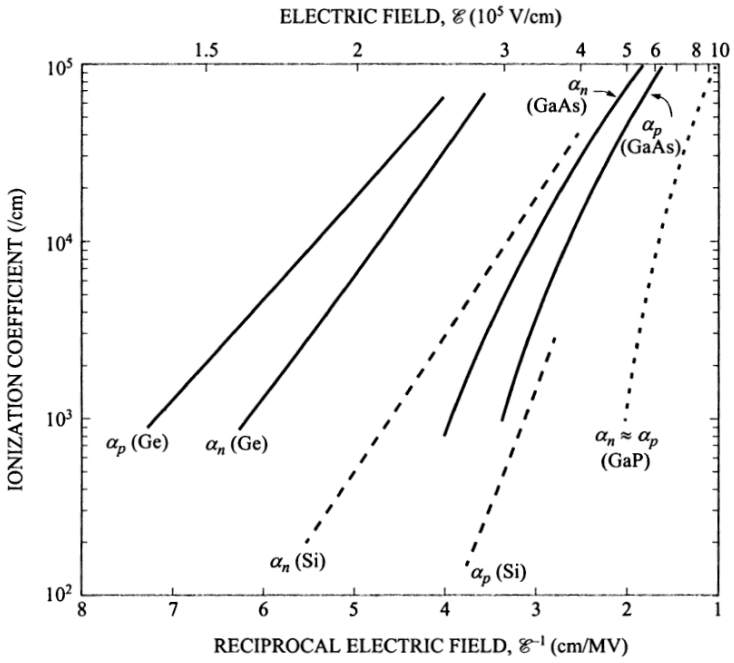

Figure 2.6: Logarithmic scaled impact ionization versus reciprocal electric field for different semiconductor materials [20].

- Linear mode: At moderate bias voltage mainly electrons contribute charge multiplication while the impact ionization coefficient for holes is to small. If an electron-hole pair is produced in the p-region, it drifts towards the cathode. Due to the high field the electrons gain enough energy to generate secondary electron-hole pairs which leads to an avalanche multiplication of electrons. A charge multiplication with a gain of $10^2 - 10^3$ is reached. The produced holes drift to the anode, but does not cause further ionization due to the smaller impact ionization coefficient α_p. Consequently, the avalanche propagates only in the direction of the electrons and the charge amplification ends, once all electrons have left the multiplication region. Operating an APD at moderate bias voltage is called linear mode, since the measured current I_a is proportional to the number of incident photons:

$$I_a = G \cdot I_\gamma$$

  where I_λ is the current of the incident photons and G the gain of the device.

- Geiger-mode: When the applied voltage across the junction is higher than the breakdown voltage, the electrical field is high enough that also holes contribute for charge multiplication. In this case, the avalanche process is no longer restricted in proximity to the multiplication regions. If an avalanche is triggered, it propagates in both directions and extends to the whole field region. During this process, which is referred to as avalanche

breakdown, the avalanche yields a growing current through the device. Due to the internal resistance R_{int} of the sensor, this will cause a voltage drop at the p-n junction. This leads to a steady state of the breakdown current. During this time, an APD is hence not sensitive to subsequent photons unless the breakdown has been stopped. Therefore, a passive quenching mechanism is implemented. The diode is connected in series to a large quenching resistor. When an avalanche breakdown is triggered, the diode capacitance C_D discharges and the current I flowing through the quenching resistor R_q causes the voltage of the APD to drop below the breakdown voltage U_{bd}:

$$U_{ADP} = U_{bd} - R_q I.$$

The avalanche process is stopped and the diode is recharged with the time $R_q C_D$. Hence the quenching resistor protects the diode by limiting the current of the APD and stops the avalanche process. An APD operating above the breakdown voltage U_{bd} is working in "Geiger-mode" leading to a gain between $10^5 - 10^6$. Due to the high gain, a single photon can trigger an avalanche breakdown of the whole device.

2.2.3 Silicon photomultiplier

A silicon photomultiplier (SiPM) is a new photon counting device built as an array of Geiger-mode avalanche photo diodes (GAPD). The SiPM depicted in figure 2.7 joins 1600 pixels over an area of $1 \times 1\,mm^2$ on a common silicon substrate. All pixels with pixel size of $25 \times 25\,\mu m^2$ are connected by aluminum metalization.

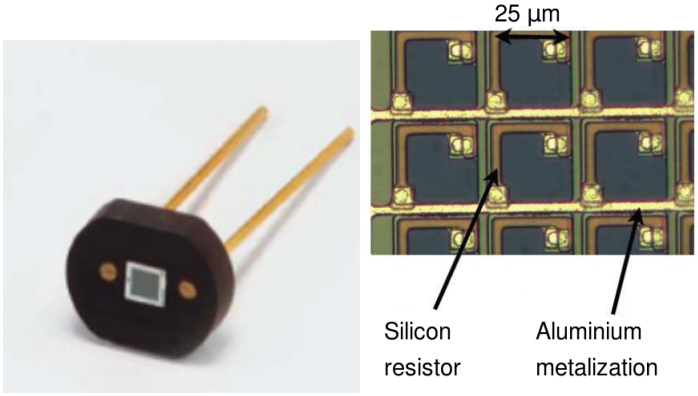

Figure 2.7: $1 \times 1\,mm^2$ SiPM produced by Hamamatsu (left) [3]. The pixel size amounts to $25 \times 25\,\mu m^2$. Microscopic image of pixel surface (right) [21].

The dynamic range of an GAPD is limited due to the recovery time where an APD is hence not sensitive to subsequent photons. The dynamic increases by using multiple pixels for the same surface. A drawback is the insensitive area between the pixels where no photons can be detected. Since each pixel operates above the breakdown voltage, a gain of $10^5 - 10^6$ can be obtained. A quenching resistor is connected to each pixel in order to stop the Geiger discharge. Each pixel operates in digital switching mode since the output of an GAPD is the same, regardless of the amount of photons which triggered the avalanche. The total output signal of the SiPM is the total sum of all fired APD pixels.

Figure 2.8 shows the topology (left) of a single pixel and the corresponding electric field profile (right). If the APD is working in Geiger mode, a high electric field is produced, in the Geiger region, between the few micrometer thin layer of p^+ and n^+-doped[1] material. Incident

[1] + and - refers to a high or low doping level

photons in this region are absorbed and trigger an avalanche. The electrical field in the drift region between the p^- and p^+-type substrate is to small for impact ionization. Hence, produced electrons in this region will drift to the Geiger region where it can trigger an avalanche breakdown. The two guard ring made of n^- silicon reduces the electrical field close to the edge of each pixel, where impurities could lead to unwanted avalanche breakdown. The surface of the pixels is cover with a thin layer of anti-reflecting SIO_2 for protecting purposes.

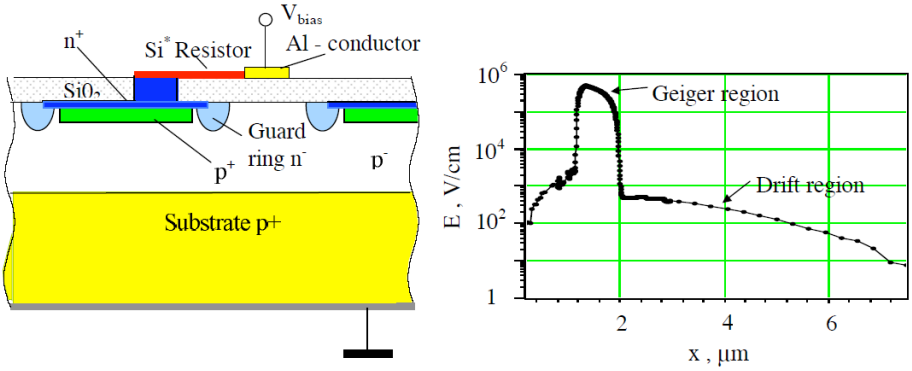

Figure 2.8: Topology (left) and electric field profile (right) of a single pixel of a SiPM operating in Geiger mode [22].

Figure 2.9 (left) shows the APD circuit in detection mode when the pixel is charged up to $U > U_{bd}$. The diode will remain in this state until a photon initiates a discharge resulting in a large current through the device. Each pixel consists of a quenching resistor R_q[2] connected in series with an APD. Figure 2.9 (right) describes the situation during breakdown where the C_{pix} represents the capacitance of the p-n junction. Using the formula $Q = C \cdot U$, the charge flowing out of the capacitor during discharge can be calculated as follows:

$$Q(t) = C_{pix}(U - U_{bd})(1 - e^{\frac{-t}{R \cdot C_{pix}}}) \tag{2.2}$$

The quenching resistor ($R_q \gg R_{int}$) quenches the current and causes the pixel capacitance C_{pix} to recharge with a time constant of

$$t_c = C_{pix} \cdot R_q. \tag{2.3}$$

During breakdown the pixel is insensitive to photons. For low photon fluxes the probability, that several photons hit the same pixel at the time, is small. In this case the response of the MPPC is approximately linear. If the number of incident photons becomes closer to the number of pixels of an MPPC, the probability increases that photons cannot be detected due to the recovery time of the pixel. This effect is referred to as saturation and reduces the number of fired pixel for high photon fluxes.

The pixels of a MPPC underlie fluctuations concerning the quenching resistor and doping concentration due to the production process. This has an effect on the breakdown voltage and pixel capacitance and consequently the gain of each pixel. This fluctuations in the response of each pixel is referred to as excess noise.

[2] Usually the quenching resistance ranges between several hundred $k\Omega$ and a few $M\Omega$.

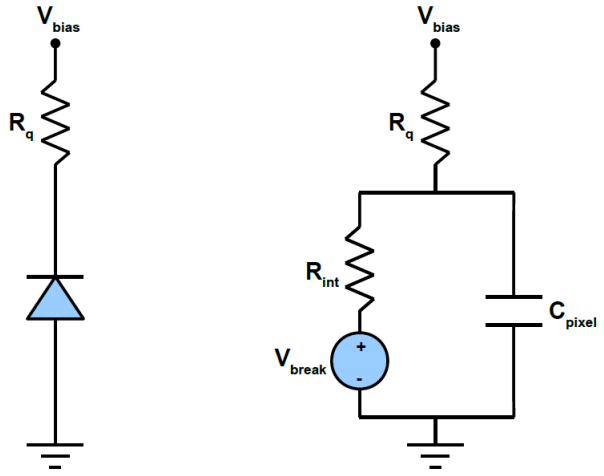

Figure 2.9: Depiction of an APD in detection mode when the voltage is higher than the breakdown voltage (left). During breakdown the the quenching resistor functions as a virtual open circuit on the timescale of discharge and then causes the pixel to recharge again (right).[23]

Other important properties of a SiPM include: Photon detection efficiency, dark rate, cross-talk and after-pulse:

- Photon detection efficiency (PDE): The PDE is the fraction of detected incident photons. It can be expressed by the following equation

$$PDE = QE \cdot F_g \cdot P_a. \tag{2.4}$$

  The geometrical factor F_g is the fraction of active surface to the total surface of the SiPM. F_g depends on the size and amount of pixel. The area occupied by silicon resistors and aluminum metalization connects all pixels and is insensitive to photons. This area increases with the amount of pixels and hence reduces F_g. The avalanche probability (P_a) is the probability that an avalanche breakdown occurs from an incident photons. This factor increases with increasing voltage over breakdown $\triangle U = U - U_{bd}$ (cf. figure 2.10 (left)). The quantum efficiency (QE) is the percentage that an incident photon produces an electron-hole pair, which depends primarily on the wavelength of the photon. The wavelength dependence of the PDE is depicted in figure 2.10 (right). For $U = 2.1\ V$, the PDE wavelength dependence has a peak absorption in the blue region.

- Dark rate: Charge carriers are not generated from photon absorption alone. Even in absence of light, charge carriers can be produced and trigger an avalanche which cannot be distinguished from a signal induced by a photon. The two principal effects responsible for the dark rate are thermal excitation and tunnel excitation. The thermal energy for room temperature is $E_{th} = k_b T = 0.026\,eV$, which is much smaller than the energy band gap of silicon ($E_{gap} = 1.14\,eV$). Hence, direct transitions are suppressed, however, electrons can also get excited by a two-step transition involving intermediate states within the forbidden energy range. Impurities and crystal defects cause a band structure disorder and hence introduce intermediate energy states. Tunnel excitation refers to the quantum mechanical phenomenon of an electron tunneling with a certain probability through a potential wall. In case of the SiPM, the band gap is the potential wall. Hence the tunnel probability increases with increasing electrical field and decreasing band gap.

- Afterpulse: An afterpulse is a spurious pulse following the real signal within a certain time. This occurs when generated carriers are trapped due to crystal defects during an avalanche breakdown. If they are trapped longer than the recovery time of one pixel, their release will appear as a single photon pulse after the real signal.
- Crosstalk: When an avalanche breakdown occurs, photons are produced due to carrier recombination, Bremsstrahlung and intraband transitions. These photons can enter neighboring pixels and can create a secondary avalanche process if their energy is sufficient. This phenomenon is referred to as "crosstalk".

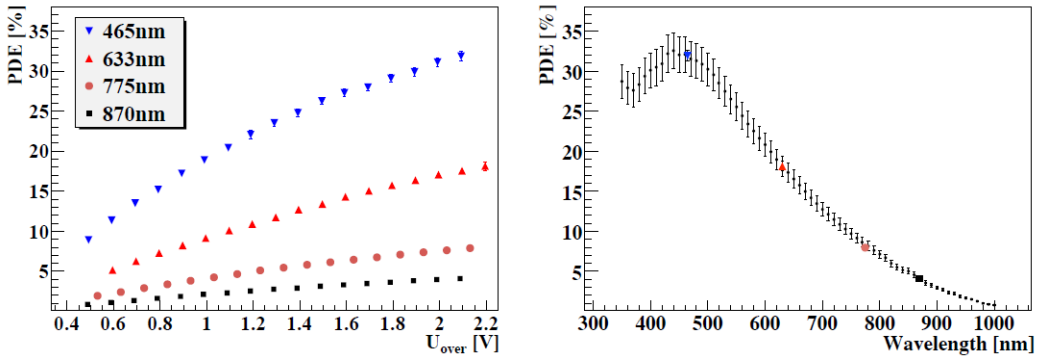

Figure 2.10: PDE of 3600 pixel SiPM produced by Hamamatsu as a function of $\triangle U$ for different wavelength (left) and wavelength for $\triangle U = (2.15 \pm 0.05)\,V$ (right), both at $T = 25\,^{\circ}C$. [24]

Chapter 3

The PET test device

This chapter describes the PET test device used in this work, its components and their basic principle of operation. The detector consists of two modules (see figure 3.1 (left)) containing small size LFS crystals individually read out via MPPCs. The two PET detector modules are mounted on two opposing support rails for translation from $3\,cm$ up to more than $20\,cm$ with respect to the center of the PET test device (see figure 3.1 (right)). Both support rails are mounted on a turn table which is steered by a rotation stage and allows rotation around the center. One support rail can also be rotated from $-70°$ to $70°$. The MPPCs of the detector heads are powered by two multi-channel high voltage modules, which allows to adjust the voltage for each channel individually. The data acquisition (DAQ) is performed by an analog-to-digital converter module (ADCM).

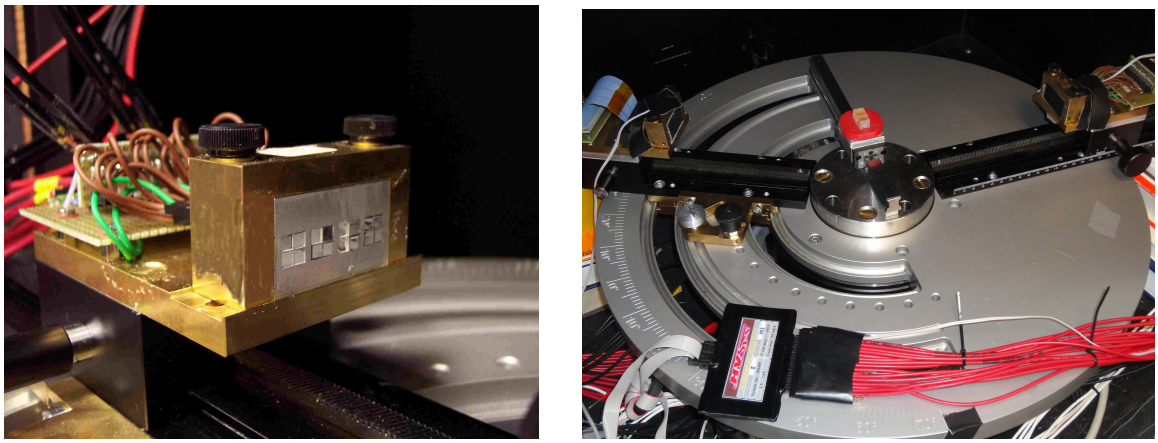

Figure 3.1: Detector head with crystals coupled to MPPCs (left). Experimental setup of the PET test device (right)

Each of the two detector modules comprises of four submodules (illustrated in figure 3.2) containing 2×2 arrays of $3 \times 3 \times 15\,mm^3$ polished LFS crystals, each read out by a $3 \times 3\,mm^2$ 3600 pixel MPPC. To improve the light transport from crystal to MPPC, they are optically coupled using optical grease. The opposite side of the crystal is covered with reflective foil. The crystals are inserted in an aluminum structure with electrical eroded cavities. The individual crystals of each array are separated by a $100\,\mu m$ thick wall.

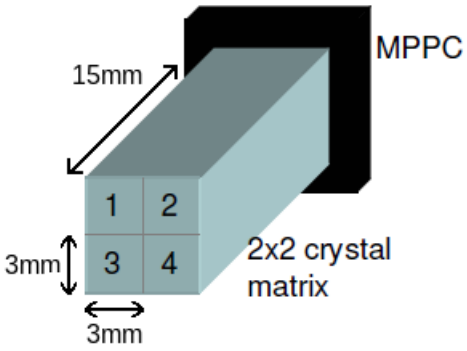

Figure 3.2: Submodule consisting of 2×2 matrix of scintillators read out by a MPPC array.

3.1 Properties of LFS

Lutetium Fine Silicate [25] is used as an inorganic scintillator material in the detector device. The most commonly used crystal in PET application is LYSO. For a specific boule[1] size properties in terms of attenuation length λ, decay time τ_c, density ρ and light yield LY are quoted for LFS and LYSO in table 3.1. Both crystals show similar values for each property. The exact value of the rise time τ_r is still under investigation. Recent measurements have shown that a rise time of $100\,ps$ is realistic [26].

Material	boule size $[cm]$	$\lambda\,[cm]$	$\tau_c\,[ns]$	$\rho\,[\frac{g}{cm^3}]$	LY [%]
LFS	$\varnothing\, 9 \times 25$	1.12	36	7.4	80-85
LYSO	$\varnothing\, 7.5 \times 15$	1.12	41	7.1	70-80

Table 3.1: Properties of LFS and LYSO. [25]. The light yield is quoted with respect to the light yield of NaI:TI.

The emission spectrum of LFS in figure 3.3 shows a peak of emission intensity in the blue and violet spectral region.

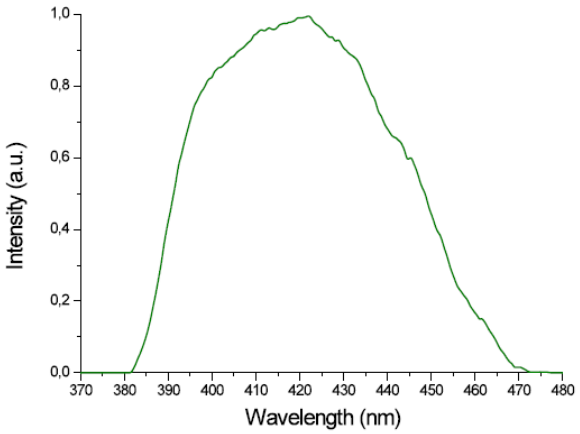

Figure 3.3: The emission spectrum of LFS with peak emission wavelength of $420\,nm$ [27].

[1] A boule is a single-crystal ingot, which is cut into circular wafers and polished afterwards. The size is quoted in diameter times length.

3.2 Multi-pixel photon counter

An multi-pixel photon counter is a silicon based photodetector, also called silicon photomultiplier (see subsection 2.2.3), capable of detecting single photons [3]. MPPCs have been tested in the detector device, due to several advantages to APDs and PMTs, such as much lower bias voltage. Another advantage to APDs are higher gain and stability in terms of gain dependence of temperature and bias voltage. In comparison to PMTs, the MPPC benefits from the insensitivity to magnetic fields and smaller size [28]. The smaller size allows for a higher amount of MPPCs to cover the same area. Thus, the granularity and hence the spatial resolution of the detector improves. The only drawback to this is the increase of the dead area between the MPPCs where no photons can be detected. In the PET detector device, arrays of 2x2 MPPCs are used, with properties listed in table 3.2. The PDE is depicted in figure 2.10 and shows a peak absorption for photons in the blue and violet region for $\triangle U = 2.1\,V$ with a PDE around 30 %. This matches the emission spectra of LFS (cf. figure 3.3), which is peaked in the same region, resulting in a high number of fired pixel with respect to the deposited energy in the crystal.

Type (size [mm^2])	$U\,[V]$	Dark Rate $[Mcps]$	Pixel Size $[\mu m^2]$	Gain $[10^5]$
2×2 array 3600 pixel ($3 \times 3\,mm^2$)	71.0	6-10	50×50	7.5

Table 3.2: Properties of 2×2 array MPPCs. The gain is quoted for $\triangle U = 1.3\,V$ and $T = 25\,°C$ [3].

3.3 High voltage module

Two high voltage power supply modules (see figure 3.4), each consisting of 16 connectors, provide the power supply for all 32 MPPCs. The principle feature of the system is high stability of negative output voltages with fluctuation less than 0.01 % from 0 to $150\,V$, with current limitation of $0.1\,mA$ [29]. Several HV modules can be connected via one USB bridge to the USB port of a computer. The remote control allows to adjust the bias voltage for each channel individually. The HV module is also equipped with a temperature sensor. This is crucial for long-time measurements, where voltage adjustments for changes in temperature are required (see section 5.3.3).

Figure 3.4: 16 channel HV module connected to USB bridge

3.3.1 Calibration of HV modules

The bias voltage of the MPPCs is provided by two HV modules and adjusted in Arbitrary Digit Unit (ADU) steps. Each channel has to be calibrated from ADU to volts for further measurements with the HV module. This is performed by the setup in figure 3.5 (left). The HV module is steered by a computer, which sets a voltage to each channel of the module. The

channel is connected in series via a resistor R to an Ampere meter, which measures the current. Due to the high resistance $R = 100.6\,M\Omega$, other small resistance effects can be neglected and the voltage can be calculated by Ohm's law to $U = R \cdot I$. The calibration data are extracted from a fit of a linear function of $U[V]$ versus $U[ADU]$. Figure 3.5 (right) shows the linear correlation of U in volts to U in ADU for channel 1.

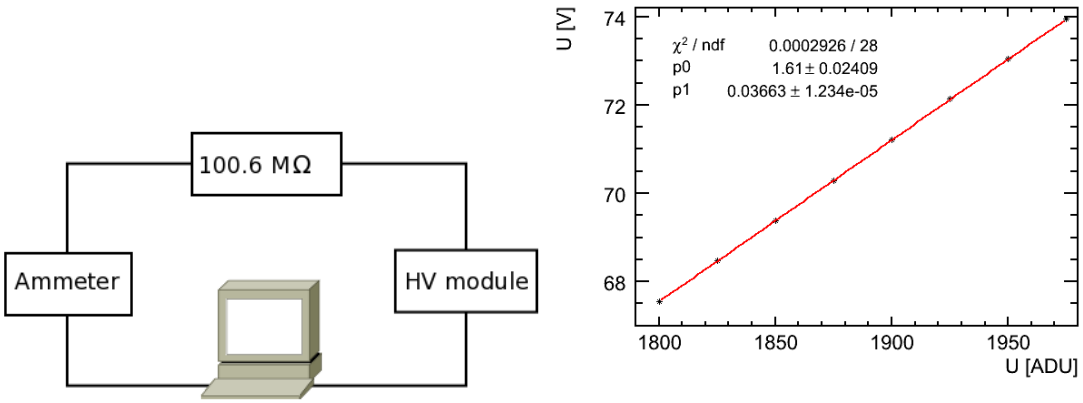

Figure 3.5: setup of HV calibration measurement (left), Calibration line of $U\,[V]$ versus $U\,[ADU]$(right)

The slope of the fit for each channel is depicted in figure 3.6 (left). The slope of each channel is nearly equal, with an RMS of less than 1 % around the mean of $36.3 mV/ADU$. The slope of each channel is the accuracy of the HV module, since the voltage can not be adjusted more precisely than in ADU. The channel-to-channel homogeneity can be described by figure 3.6 (right) which shows the distribution of U[V] for each channel for the same $U\,[ADU] = 1900\,ADU$. The mean value amounts to $70.5\,V$ with a RMS of $0.5\,V$, which shows a channel-to-channel deviation from less than 1 %, as quoted by the company. The calibration data is used to apply the voltage in volts in all following measurements.

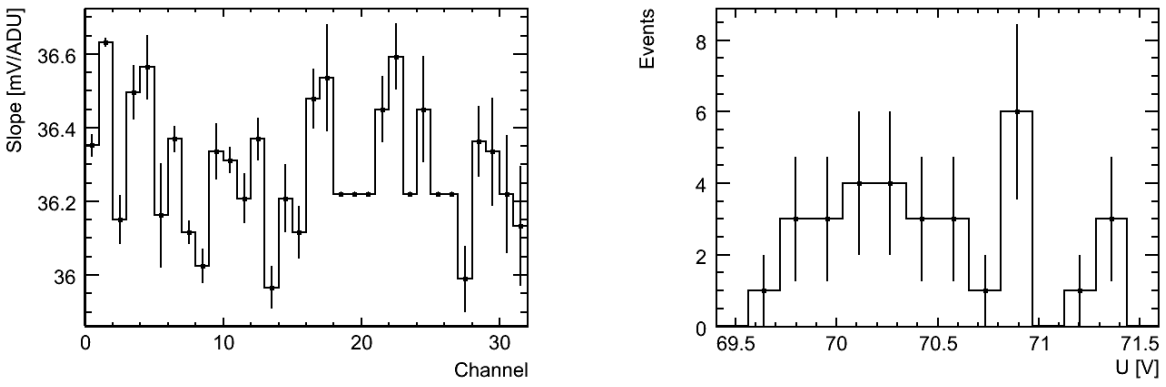

Figure 3.6: Extracted from fit on a linear function of each channel: slope (left). Distribution of $U\,[V]$ for each channel for $U\,[ADU] = 1900\,ADU$ (right).

3.4 Analog to digital converter module

ADCM-16 is a 16-channel 10-bit analog to digital converter (ADC) board with a signal processing core [30]. The data acquisition hardware utilizes high speed ADC by recording the amplitude of the signal every $10\,ns$ for each channel. The ADCM data acquisition software is also capable of analyzing data online. The baseline is subtracted and the integral, width and time are presented in online histograms and can also be stored in a data file. It is also possible to store raw which consists of data frames each containing one waveform. A data frame records a sample each $10\,ns$ within an adjustable time range. The ADCM provides first and second level trigger logic to derive coincidences between channels within a specific time window.

3.4.1 Coincident measurement with ADCM

A key feature of a PET scan is the determination of coincidences between channels. For this purpose, two ADCM modules with 16 channels are used. To derive coincidences between all recorded signals during data taking, first and second level trigger logic is performed. A screenshot (see figure 3.7) of the data acquisition software platform is used to illustrate the working principle of the ADCM.

Two channels are in coincidence when both signals cross the threshold within a specific time window. The identification is realized by first group of triggers γ and second group α. When a signal of a γ-trigger set channel crosses the threshold, the intersection point is set as the zero in time. A certain variable time window with respect to the zero point opens. If the signal of a α-trigger enabled channel crosses the threshold within the time window, it is stored with the channel from trigger γ as one coincidence event. Each event consist of both channel IDs and the integral of the two waveforms. The zero suppression setting ensures that only coincidence events are recorded by the ADCM. Events below the threshold are suppressed.

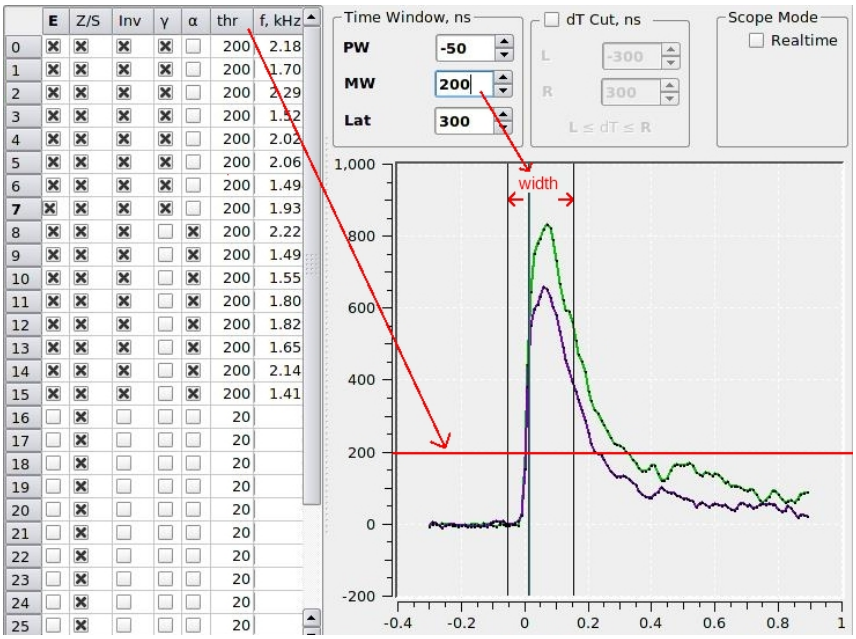

Figure 3.7: Screenshot of ADCM display on a computer during data acquisition. Abbreviations: E: Enabled, Z/S: Zero suppression, inv: Inverted signal, γ/α: Trigger, thr: Trigger threshold, f: Frequency of events in kHz

3.4.2 Output of data acquisition software

The data acquisition software integrates the signal by summing up the amplitude during a specific time range and subtracting the baseline from this result. The integration range can be set for each channel individually with respect to the zero point of the waveform. The unit of the amplitude A_n is measured in $0.1\,mV$ and the time in $10\,ns$ steps. Hence the amplitude of the ADCM can be expressed as: $A_n = U \cdot N_n$, where $U = 0.1\,mV$ and N the amount of ADCM channels of the amplitude. The ADCM output A is the integral divided by the amount of $t = 10\,ns$ steps I :

$$A\,[pVs] = \frac{t}{I}\sum_{n=1}^{n=I} A_n$$

To determine the charge output Q_{ADCM} of one waveform, the output has to be multiplied with I and divided by the termination resistance $R = 50\Omega$:

$$Q_{ADCM}\,[pC] = \frac{A \cdot I}{R} = \frac{tU}{R}\sum_{n=1}^{n=I} N_n. \tag{3.1}$$

The quotient before the sum describes the sensitivity of the ADCM $S_{ADCM} = 20\,fC/ch$, which leads to

$$Q_{ADCM} = S_{ADCM}\sum_{n=1}^{n=I} N_n. \tag{3.2}$$

To crosscheck this assumption, waveforms have been analyzed via the ADCM DAQ and a charge to digital converter (QDC[2]). The measurement is performed with the following setup (see figure 3.8): The pulse generator[3] creates two signals. Signal 1 generates a gate-width of 820 ns. Signal 2 is shaped with another pulse generator[4] and integrated by the QDC in this gate. The same signal 2 has also been measured by the ADCM and converted to charge by equation 3.1. The integral Q of the QDC must be corrected by subtracting the pedestal P, which is the sum of the electronic noise in the integration range. This result has been converted from QDC channel to charge by multiplying with its sensitivity $S_{QDC} = 50\,fC/ch$:

$$Q_{QDC} = (Q - P)S. \tag{3.3}$$

[2]Charge to digital converter Lecroy1182[31]
[3]Stanford Research systems Module DG 5353 Digital/Pulse generator
[4]hp 8082A pulse generator

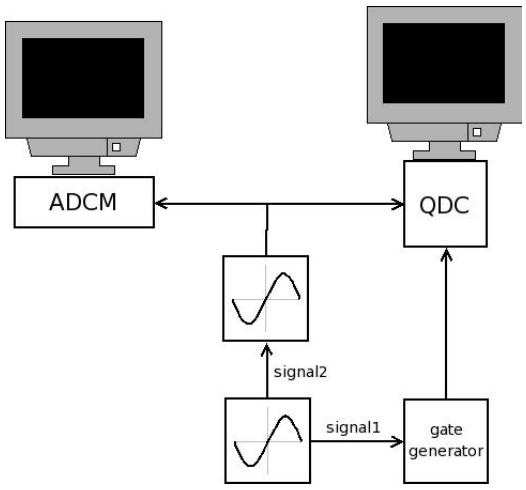

Figure 3.8: Setup to compare data acquisition of ADCM and QDC. The same pulse is integrated in the same range of 820 ns by both DAQ modules.

Figure 3.9 shows Q_{QDC} and Q_{ADCM} measured for the same pulse. The orientation of data points around the line through origin with gradient 1 indicates how well both charge measurements match. The deviation of Q_{QDC} from Q_{ADCM} is depicted in figure 3.9(right). For small values of Q_{ADCM} the deviations goes up to 14 % while for $Q_{ADCM} > 200pC$ both integrals are in good agreement with each other.

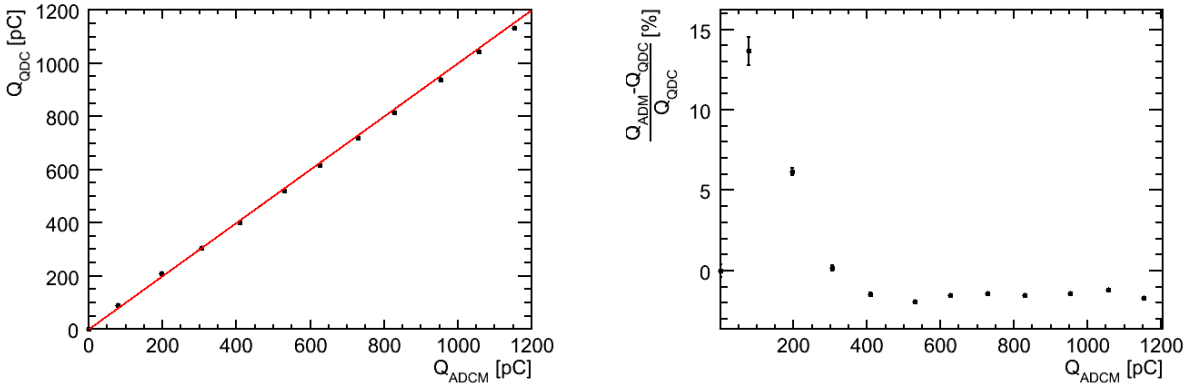

Figure 3.9: Same signal measured in unit charge with QDC and ADCM (left), residual plot of Q_{QDC} to Q_{ADCM} (right).

3.5 Description of Sodium-22 decay

Sodium-22 (^{22}Na) is a radioactive isotope of the metallic element sodium with a half-life of 2.6 a. ^{22}Na decays to 90 % via $^{22}_{11}$Na ->$^{22}_{10}$Ne $+e^{+}+\nu_e$ and 10 % electron-capture to an excited state of ^{22}Ne which returns to the ground state by releasing energy in form of a 1.277 MeV photon (cf. figure 3.10). The positron range (see chapter 1) of the emitted β^{+} depends on the kinetic energy of 33 keV which is rather small compared to common used radionuclides in PET (cf. table 1.1). Therefore, ^{22}Na is suitable for studies with the PET prototype in order to achieve a good spatial resolution. The energy spectrum of the decay of ^{22}Na shows two emission peaks at 511 keV and 1.277 MeV. The first peak shows the position of the photoelectric peak while

the second peak can only be used for calibration purposes.

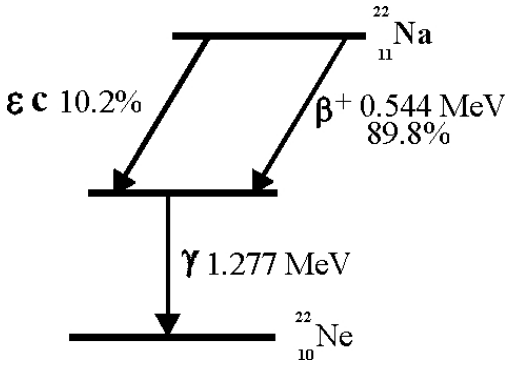

Figure 3.10: Decay scheme of ^{22}Na.[32]

Chapter 4

MPPC Characterization

The photo-detection of the crystals in the PET test device is performed by 32 MPPCs manufactured by Hamamatsu. The manufacturer quotes several important properties for each series of MPPC. The most important properties, like gain and dark rate, are specified at a certain bias voltage for each MPPC. In the following measurements, the MPPC will be characterized concerning the gain and dark rate and compared to the data of the manufacturer Hamamatsu. The results from the gain measurement are also used to determine the pixel capacitance which is essential to calculate the time constant of each MPPC using equation 2.3. The quenching resistor is derived from the forward bias region of the IV-curve. The time constant has also been extracted from an exponential fit on the falling edge of the waveform to verify the quality of the MPPC characterization measurements.

4.1 Gain Calibration

A characteristic property of the MPPC is the gain which, is the amount of charge carriers generated by one fired pixel. The gain is essential to calculate the number of detected photons (see 5.1), the pixel capacitance of an MPPC and for time resolution measurements to trigger on the first photon arriving. For latter, it is important to set a threshold below the amplitude of the signal which is proportional to the gain (see subsection 5.3.2). In this experiment, all 32 MPPCs of the detector device will be investigated concerning temperature and voltage dependence of the gain.

4.1.1 Experimental setup

The gain of an MPPC was measured as a function of the applied bias voltage by the following setup (cf. figure 4.2). The rectangular pulse of pulser 1[1] is tuned by an analog pulse generator pulser 2[2] to drive an LED. The light of the LED is transmitted along an optical fiber into the lightproof box where it is aligned towards the surface of the MPPC. The light intensity of the LED attenuated with a neutral density filter (NDF) and tuned with pulser 2 in a way, that every light pulse has a low intensity in order to detect single photons with the MPPC. The Keithley power supply [33] is steered by a computer via a USB-GPIB (General Purpose Interface Bus) adapter to automatize the bias voltage of the MPPC. When a light pulse hits the surface of the MPPC, an avalanche breakdown occurs in the corresponding pixel. The generated

[1] Stanford Research systems Module DG 5353 Digital/Pulse generator
[2] hp 8082A pulse generator

charge is amplified[3] by a factor of 20 and integrated by the QDC [4]. In order to integrate the signal, the integration of the QDC is triggered by the same pulse generator used to operate the LED. The gate generator sets the integration range of the QDC when it is triggered by the discriminated pulse of pulser 1. A temperature sensor is also installed in the lightproof box to record the temperature during data taking. Bias voltage, temperature and charge spectrum (single photoelectron spectrum) are stored for each measurement.

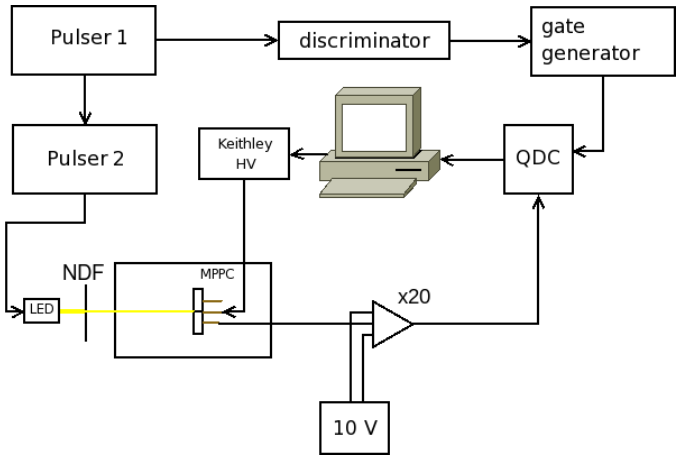

Figure 4.1: Setup for gain measurement

4.1.2 Determination and optimization of gain

Figure 4.2 (left) shows a single photoelectron spectrum obtained by the setup described above. The charge spectrum contains $2 \cdot 10^5$ events which have been integrated by the QDC. Each peak in the spectrum corresponds to a certain number of photoelectrons (p.e.). The first peak is the pedestal peak which contains all events without photoelectrons. The second peak corresponds to the charge output of one p.e., and so forth. The peaks are clearly separated but smeared due to electronic noise and statistical fluctuations of the gain of each pixel during an avalanche breakdown. This effect, called excess noise (see subsection 2.2.3), increases for a larger amount of fired pixels.

Since the amount of detected photons is equal to the peak order of the spectrum, the distance between two peaks corresponds to the charge output of one MPPC pixel which is the definition of the gain. Due to the continuous sequence of the peaks, a Fourier transform has been used to compose the distances between the peaks into a frequency. The harmonic at zero shows the electronic noise while the second peak, or first harmonic (cf. figure 4.2 (right)) corresponds to the frequency of single photoelectric peaks. Hence, the gain in QDC channel G_{ch} can be calculated by dividing the range ($1000\,1/ch$) of the spectrum by the mean extracted form a Gaussian fit on the first harmonic. The gain value G is derived from the QDC sensitivity $S = 50\,fC/ch$, the unit of elementary charge $e = 1.602 \cdot 10^{-4}\,fC$ and the amplification factor $A = 20$:

$$G = \frac{S \cdot G_{ch}}{A \cdot e}.$$

[3] Philips scientific wideband amplifier with amplification factor 20
[4] Charge to digital converter Lecroy1182 [31]

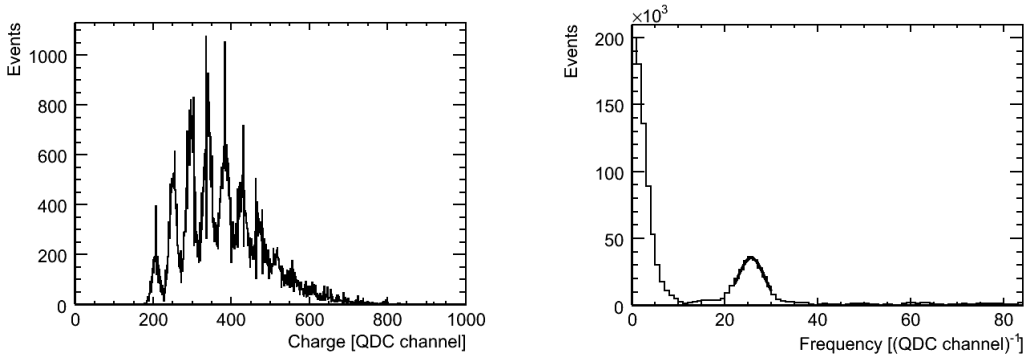

Figure 4.2: Single photoelectron spectrum in QDC channel (left), Fourier transform of single photoelectron spectrum with Gaussian fit on the first harmonic (right).

The measured gain depends on the integration range of the QDC, which can be varied by the gate generator. In order to optimize the measurement, the gate width has been varied in order to integrate the whole charge from the MPPC, while keeping the gate width as small as possible to avoid integration of additional noise. The QDC starts to integrate the signal with a time delay of $30\,ns$ to the leading edge of the gate [31]. Figure 4.3 shows gain versus delay time for $U = 70.6\,V$ (left) and $U = 70.8\,V$ (right). Both figures show a drop in gain for a time delay of $20\,ns$ while the gain is basically constant in the range of 30 to $50\,ns$. Due to the delayed integration of the QDC, a part of the signals has not been integrated below $30\,ns$. Therefore, the time delay of $30\,ns$ has been confirmed.

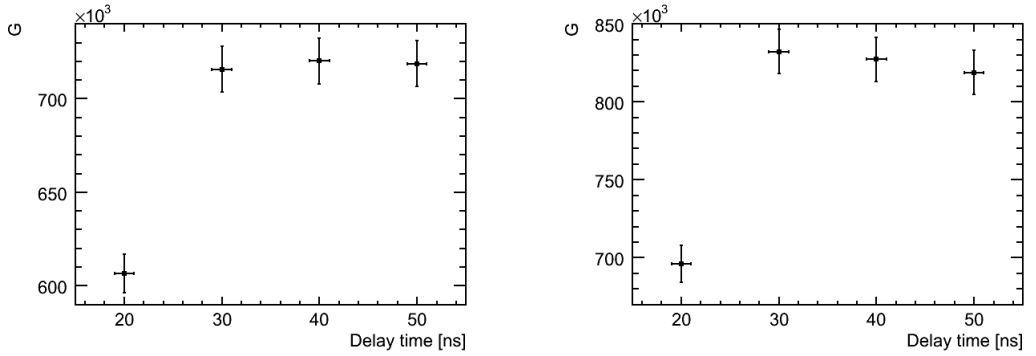

Figure 4.3: Scan of the gain over delay time for $U = 70.6\,V$ (left) and $U = 70.8\,V$ (right)

Figure 4.4 shows the graph of gain versus gate width for $U = 70.6\,V$ (left) and $U = 70.8\,V$ (right). The gain increases for larger gate widths until it reaches a plateau at $130 - 150\,ns$. To keep the amount of noise to a minimum, the smallest gate width of $130\,ns$ will be used in the following gain measurement.

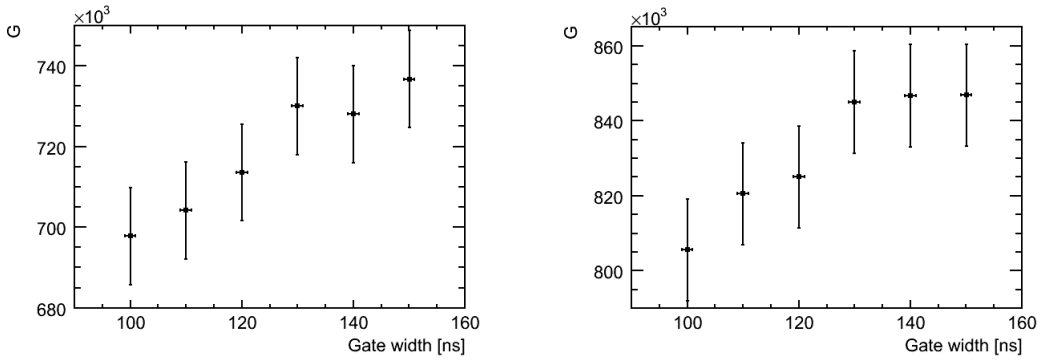

Figure 4.4: Scan of the gain over gate width for $U = 70.6\,V$ (left) and $U = 70.8\,V$ (right)

4.1.3 Voltage and temperature dependence of the gain

The gain of the MPPC depends on the applied voltage and temperature. The gain is proportional to the applied bias voltage U:

$$G(U) = a_U \cdot U + b_U.$$

The expected linear correlation between the gain and the bias voltage is depicted in figure 4.5. From the fit on a linear function, a_U and b_U can be derived. The breakdown voltage U_{bd} can be derived for $G(U_{bd}) = 0$ and calculated as

$$U_{bd} = -\frac{b_U}{a_U}$$

leading to

$$G(U) = a_U \cdot (U - U_{bd}).$$

The gain can also be calculated from formula 2.2:

$$G(U) = \frac{Q(t \to \infty)}{e} = \frac{C_{pix}}{e} \cdot (U - U_{bd}) \tag{4.1}$$

leading to $C_{pix} = e \cdot a_U$, where e is the elementary charge.

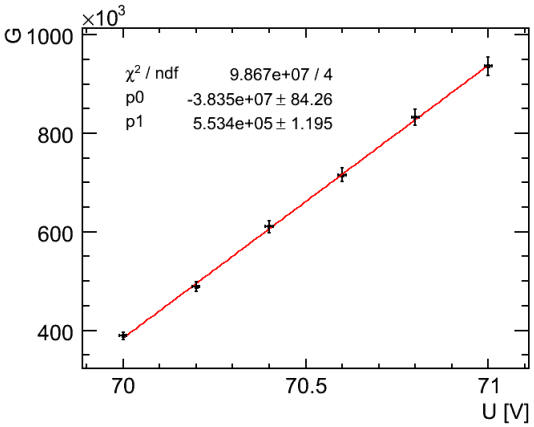

Figure 4.5: Dependence of the gain on applied bias voltage

The gain dependence on the temperature is due to the linear correlation between the breakdown voltage and temperature (cf. figure 4.6 (right)).

$$U_{bd}(T) = a_T \cdot T + b_T. \tag{4.2}$$

This leads to a description of the gain for temperature and voltage dependence:

$$G(U,T) = \frac{C_{pix}}{e} \cdot (U - U_{bd}(T)). \tag{4.3}$$

Several scans of gain versus bias voltage have been performed for different temperatures to derive the temperature dependence of $U_{bd}(T)$ for one reference MPPC. Figure 4.6 (left) shows the distribution of the pixel capacitance C_{pix} of all measurements for the same reference MPPC. Measurements where the temperature deviation $T_{dev} > 0.05\,°C$ have been excluded. The small RMS of $0.72\,fF$ is less then 1 % of the mean value $\langle C \rangle = 87.4\,fF$ and thus shows the expected independency of C_{pix} of the temperature. Therefore the determination of each breakdown voltage has been repeated with a fixed value of $C_{pix} = \langle C \rangle$.

Figure 4.6 (right) shows the expected linear correlation between U_{bd} and T. A linear fit is used to extract the values $a_T = (55.95 \pm 0.4)\,mV/°C$ and $b_T = (68.09 \pm 0.01)\,V$ of equation 4.2. Only the factor a_T is needed to correct the voltage for temperature changes (see subsection 5.3.3).

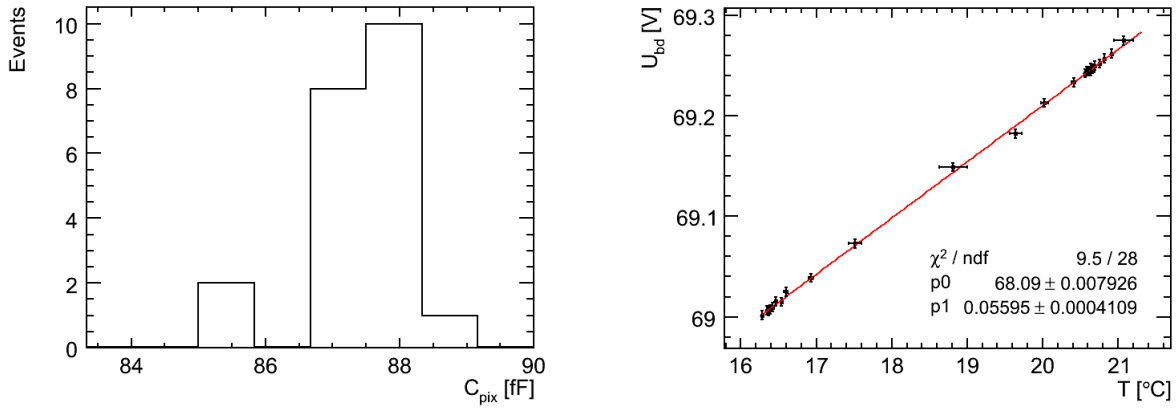

Figure 4.6: Distribution of the of the pixel capacitance for different temperatures (left). Linear correlation of U_{bd} and temperature (right). The measurement have been performed with one reference MPPC.

The essential parameters to determine the gain of an MPPC are U_{bd}, C_{pix} and a_T. With these parameters the gain can be calculated for every voltage and temperature using equation 4.3. The purpose of this measurement is to obtain C_{pix} and U_{bd} for all eight 2×2 arrays of MPPCs. To compare the breakdown voltage of all MPPCs with each other, they have to be calibrated to the same temperature $T = 25\,°C$ by

$$U_{bd}(T) = U_{bd}(T_0) + a_T \cdot (T - T_0). \tag{4.4}$$

When $U_{bd}(T_0)$ has been measured for a certain temperature T_0, it can be calculated for any other temperature. Figure 4.7 (left) shows U_{bd} for $T = 25°C$. The mean value amounts to $69.6\,V$ with an RMS of 1 % vary which shows the uniformity of the MPPCs. Figure 4.7 (right) shows that the pixel capacitances of the MPPCs are constant within error with an RMS of 2 % for a mean value of $90.7\,fF$.

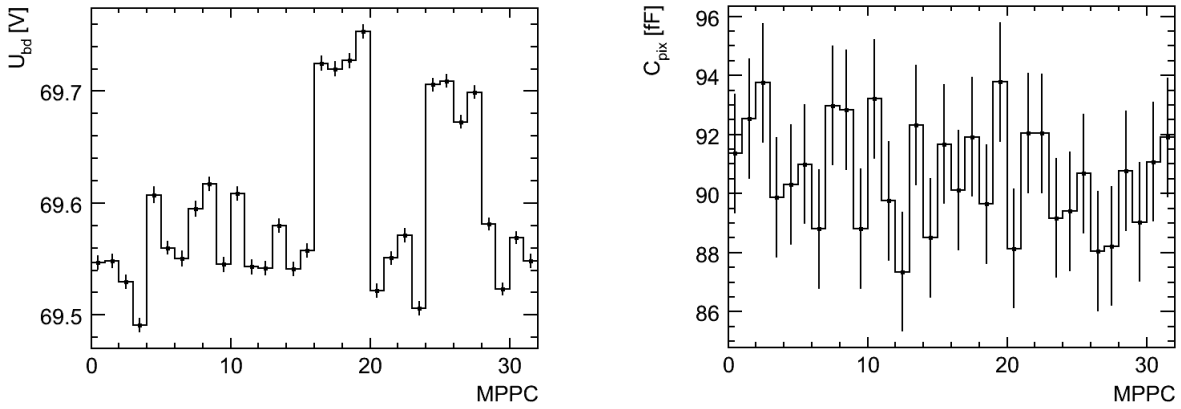

Figure 4.7: U_{bd} at $T = 25\,°C$ (left) and C_{pix} (right) of each MPPC.

The results of the measurement can be compared with the data[5] claimed by the manufacturer (see figure4.9). For this purpose, figure 4.8 (left) shows the gain for $U = 71\,V$ at $T_0 = 25\,°C$. The solid line shows the results from the measurement, and the dashed line, the gain measured by Hamamatsu. An offset of 6 % of the measured gain value appears between the lines while the shape of both lines looks similar. The offset of $5 \cdot 10^4$ is a hint of a systematic error, which could be a different integration range or the uncalibrated temperature sensor used in this measurement. Assuming a $10\,ns$ smaller integration range, the gain would decrease by an amount of $2.5 \cdot 10^4$ and which is half the offset. The offset corresponds to a temperature difference of $2\,°C$. Figure 4.8 (left) shows the measured gain for the same bias voltage, but temperature of $27°C$. In this case, the results from Hamamatsu and the measured data are in good agreement with each other.

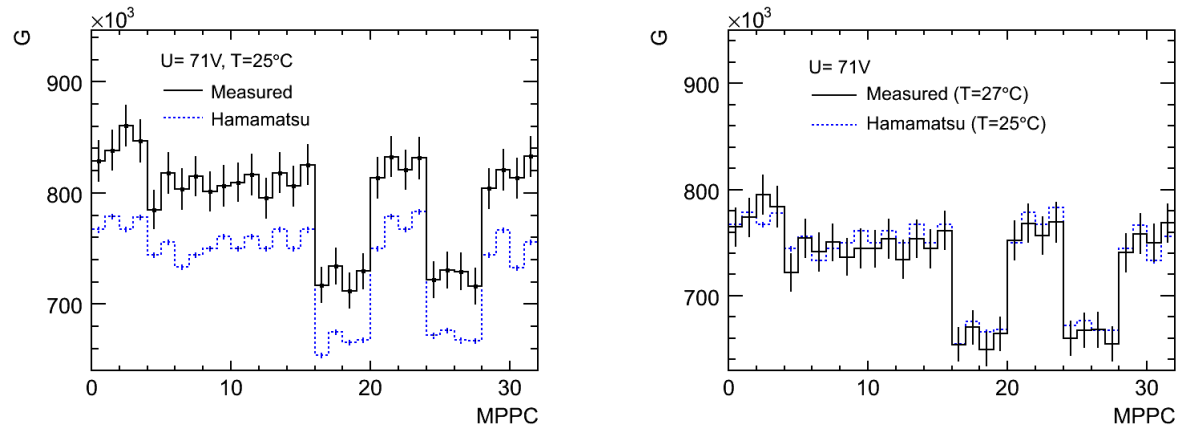

Figure 4.8: Gain for $U = 71\,V$ for each MPPC determined from the measurement (solid line) and quoted by Hamamatsu (dashed line) (left). The offset between both results corresponds to a temperature difference of $\triangle T = 2°C$. Therefore the solid line shows the gain for $T = 27°C$ (right).

[5]For each MPPC Hamamatsu quotes gain and dark rate for $U \approx 71\,V$ on the package of the MPPC array

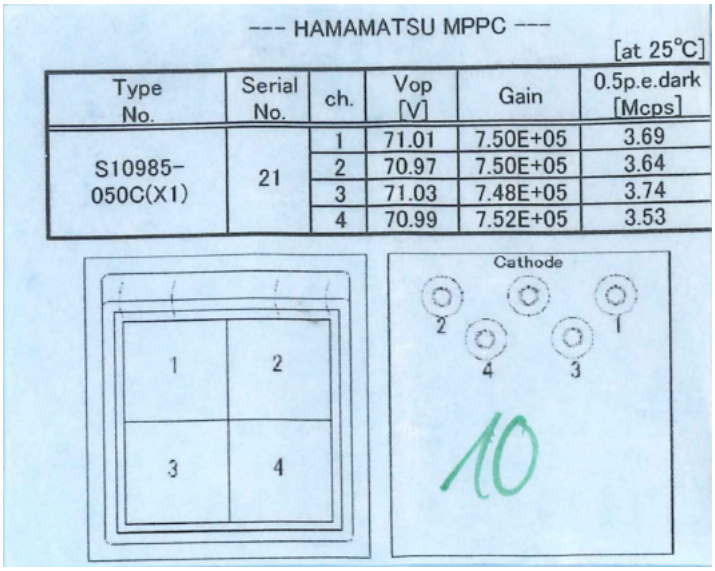

Figure 4.9: Quoted data of Hamamatsu for MPPC array 10. The gain and dark rate are quoted for $U = V_{op} = 71\,V$ and $T = 25\,°C$.

4.2 Dark rate

Besides photon detection, an MPPC pixel can also be triggered by thermal excitation or tunneling of an electron. The rate of these dark counts is a vital characteristic of an MPPC. A low dark rate reduces noise, which improves the capability of detecting single photons. This section describes the measurement of the dark rate versus $\triangle U$ for all eight MPPC arrays of the test device.

4.2.1 Experimental setup and measurement

The correlation between dark rate and $\triangle U$ have been measured with the setup described in figure 4.10. The power supply[6] of each MPPC have been operated at five different voltages from 70.4 to $71.2\,V$ in $0.2\,V$ steps and one without power supply to measure the electronic noise. The MPPC is placed inside the light tight box to avoid detection of optical photons. The output signal was amplified[7] by a factor of 50 and recorded by an ADCM (see section 3.4) which takes data frames of waveforms. One data frame of raw data contains a sample each $10\,ns$ for $240\,\mu s$. The ADCM records a new data frame when it receives a trigger signal from the pulse generator. A temperature sensor has been attached close to the MPPC. The measured temperature is required to calculate $\triangle U = U - U_{bd}(T)$ using equation 4.4 .

[6] Keithley power supply [33]
[7] Philips scientific wideband amplifier with amplification factor 50

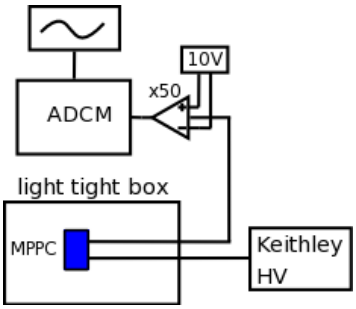

Figure 4.10: Schematic view of setup used for dark rate measurement.

4.2.2 Dark rate dependence on voltage over breakdown

In absence of light, a pulse which exceeds a threshold of $0.5\,p.e.$ is called dark count. The amount of dark counts during a certain time frame describes the rate of dark counts and is referred to as dark rate. To derive this value, a threshold scan on the raw data frames for each voltage has been performed. The rate of dark counts should decreases for higher thresholds in a step-like way. If the threshold becomes higher than one fired pixel, the rate drops typically by a factor of three and if it becomes higher than the second, the rate drops again and stays constant in between. Figure 4.11 (left) shows the rate versus threshold, subtracted by the background noise (rectangular points) where no voltage has been applied. The background events are depicted by triangle points and have rate below $1\,Mcps$, which is much lower than the total rate. The step function is just recognizable for the first fired pixels but already the second step is difficult to distinguish. This is due to electronic and excess noise which smears the signal of each fired pixel and hence complicates the separation for a various number of fired pixels. This adds up for multiple fired pixels. The rate at $0.5\,p.e.$ is taken as the dark rate for each voltage. Figure 4.11 (right) shows a linear correlation between dark rate and voltage over breakdown in a range between 0.4 and $1.3\,V$ over breakdown. The channel-to-channel distribution of the dark rate for the same $G = 7.5 \cdot 10^5$ is depicted in Figure 4.12. The mean value of the dark rate of all MPPCs is $8.1\,Mcps$ with an RMS of $0.4\,Mcps$.

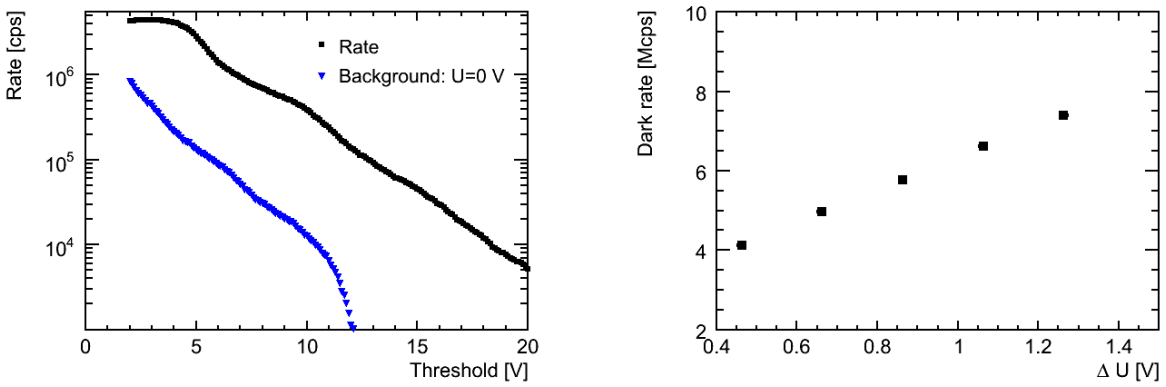

Figure 4.11: Dark count rate versus threshold for $\triangle U = 0.46\,V$ subtracted by the background events recorded at $U = 0\,V$ (left). Dark rate versus $\triangle U$ for one MPPC (right).

For an identical gain, Hamamatsu has measured a dark rate below $4\,Mcps$ (cf. figure 4.9). To crosscheck the measurement, one MPPC have been measured with a slightly different setup.

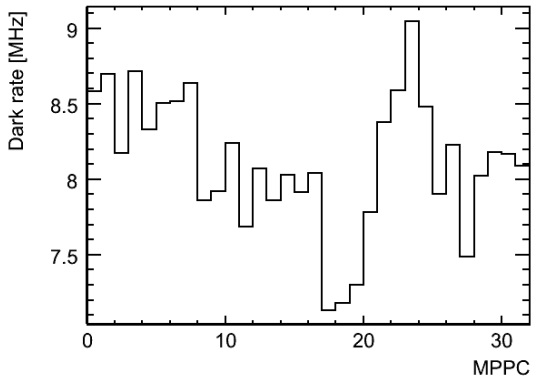

Figure 4.12: Dark rate of each MPPC for $G = 7.5 \cdot 10^5$ and $T = 25\,°C$.

The ADCM is replaced by the QDC and the integration is triggered by a pulse generator[8]. For a gate width[9] $w = 70\,ns$ random signals are integrated. Figure 4.13 (left) shows the charge spectrum at $\triangle U = 0.57\,V$. The first peak shows the pedestal and the second peak corresponds to the integral of one fired pixel. The vertical line shows the threshold at the charge $Q_{0.5}$ of $0.5\,p.e.$. The dark rate DR can be calculated as follows:

$$DR = \frac{N_{0.5}}{N \cdot w}$$

where $N_{0.5}$ is the number of events with $Q > Q_{0.5}$ and $N = 2 \cdot 10^5$ the total number of events. The results of the measurement with the ADCM and QDC are presented in figure 4.13 (right). Both dark rates are higher than the dark rate measured by Hamamatsu (cf. figure 4.9), but recently Hamamatsu has adjusted their quotation upwards to a dark rate between 6 and 10 $Mcps$ for the same gain [3]. This is in agreement with both measurements. Furthermore, the dark rate measured by the ADCM is about 1 $Mcps$ higher than for the QDC. The difference occurs from the working principle of both measurements. The ADCM measurement sets a threshold at the amplitude of the signal and the QDC at the integrated charge. The difference of both methods can occur from the handling of afterpulses. Charge carriers generated from an avalanche can be trapped due to crystal impurities. They can be released after the signal in a time window smaller than the gate width of $70\,ns$. Therefore, in the QDC measurement the original signal and the afterpulse can be counted as one event, while in the ADCM measurement they are counted as two, since signal and afterpulse have an amplitude higher than the threshold. This might explain the higher measured dark rate of the ADCM measurement, but have to be further investigated.

[8]Stanford Research systems Module DG 5353 Digital/Pulse generator
[9]This number has been subtracted by the death time of the QDC which is 30 ns (see subsection 4.1.2).

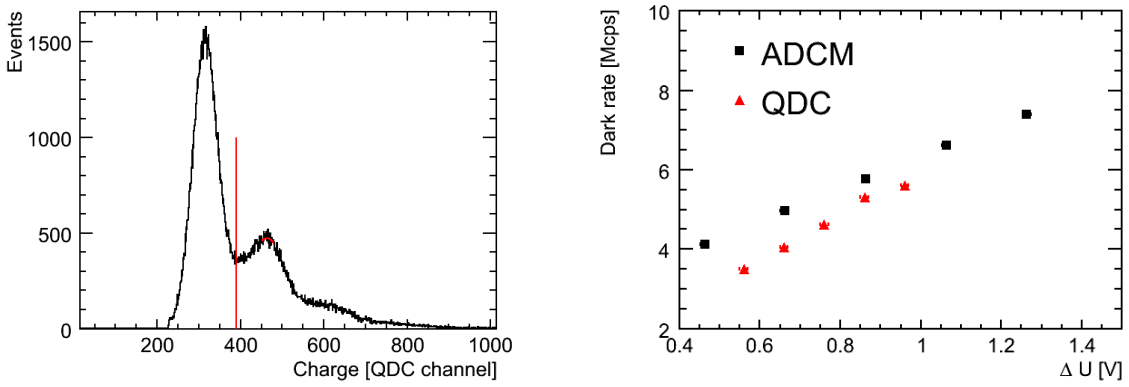

Figure 4.13: Charge spectrum of dark rate recorded by QDC for $\triangle U = 0.66\,V$ in QDC channel (left). Comparison of dark rate measurement with QDC and ADCM of the same MPPC (right).

4.3 Determination of time constant by IV-curve and waveform analysis

The time constant t_C describes the time a pixel needs to recharge after avalanche breakdown. This depends on the pixel capacitance C_{pix} and the quenching resistor R_q (see equation 2.3). C_{pix} has been determined in subsection 4.1.3 while R_q has to be determined from the forward bias region of the IV-curve. The IV-curve describes the correlation between applied voltage and current through the device. A voltage source-ammeter[10] provides the voltage to the MPPC and measures the current flowing through it (see figure 4.14).

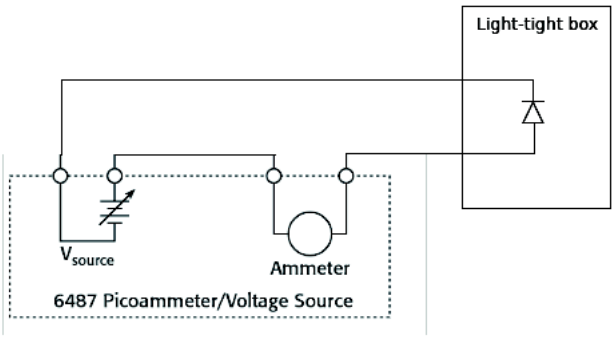

Figure 4.14: Setup of IV-curve measurement.

The reverse bias voltage higher than the breakdown voltage yields an increasing negative current in the reverse bias region as seen in figure 4.15 (left). When applying a forward bias voltage, the depletion region of the p-n junction decreases which leads to an increasing current of the electrons and holes. For larger values of the voltage, the depletion region disappears and the p-n junction is biased directly. The increase of the current is just limited by the quenching resistor, since the resistance of silicon is negligible with respect to it. The IV-curve exhibits a linear behavior which can be described by Ohm's law $dU = R \cdot dI$ (see figure 4.15 (right)). Since all quenching resistors are adjusted in parallel the total resistance R can be calculated by

[10] Keithley power supply [33]

Kirchhoff's circuit laws to

$$\frac{1}{R} = \frac{1}{R_q} + \frac{1}{R_q} ... = \frac{N_{pix}}{R_q}.$$

The slope in this region is hence related to the quenching resistor value by

$$\frac{dI}{dU} = \frac{N}{R_q} \tag{4.5}$$

where N is the number of pixels of the MPPC. The quenching resistor can be derived from the fit of a linear function on the IV-curve in this region using equation 4.5.

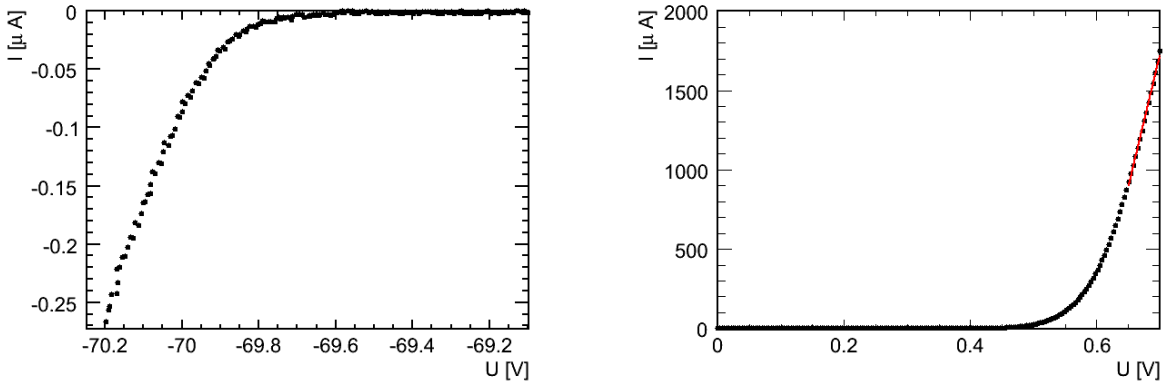

Figure 4.15: IV-characteristic for reverse (left) and forward (right) voltage. I drops in the reverse bias region when $U < U_{bd}$, which is around $-69.6\,V$. In the forwards bias region, the depletion region decreases for higher forward U until the diode is biased directly and the slope of the curve exhibits a linear behavior which is reversely proportional to R_q.

Figure 4.16 shows the quenching resistor of each MPPC. The variations of the quenching resistance are small, with an RMS of less than 1 % around a mean value of $231\,k\Omega$. Four consecutive MPPCs always belong to one 2x2 array. The last two quenching resistors of each MPPC array are approximately $35\,k\Omega$ higher than the first and second.

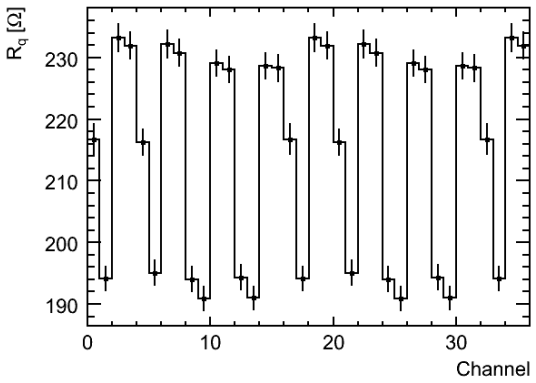

Figure 4.16: Quenching resistor R_q for each MPPC (left). Always four MPPCs belong to one array.

Figure 4.17 (left) shows the surface of an MPPC. Each of the 3600 pixels is connected by a thin layer of aluminum metalization to the readout anode. The mean distance between each

pixel and anode is about 3 mm longer for MPPC three and four since the readout is placed on the upper part of the MPPC array 4.17 (right). The longer distance of the metalization contributes to a higher internal resistance R_i which enlarges the measured quenching resistor R_q:

$$\frac{R_q}{N} = \frac{R'_q}{N} + R_i.$$

The internal resistance can be calculated to

$$R_i = \frac{(R_q - R'_q)}{N}$$

The approximated difference of $R_q - R'_q \approx 35\,k\Omega$ leads to an internal resistor of $R_i \approx 10\,\Omega$. The size of aluminum metalization can be calculated to crosscheck if the assumption is realistic. For this purpose the formula for the resistance of a wire has been used:

$$R = \frac{\sigma \cdot L}{A} \tag{4.6}$$

with L being the length, A the cross-sectional area and $\sigma = 2.82 \cdot 10^{-8}\,\Omega m$ the resistivity of aluminum. The length can be assumed to be 3 mm longer for the last two MPPCs. Assuming a square shape of the metalization, equation 4.6 leads to a width of $3\,\mu m$ which is in good agreement with the total width of one pixel being $50\,\mu m$.

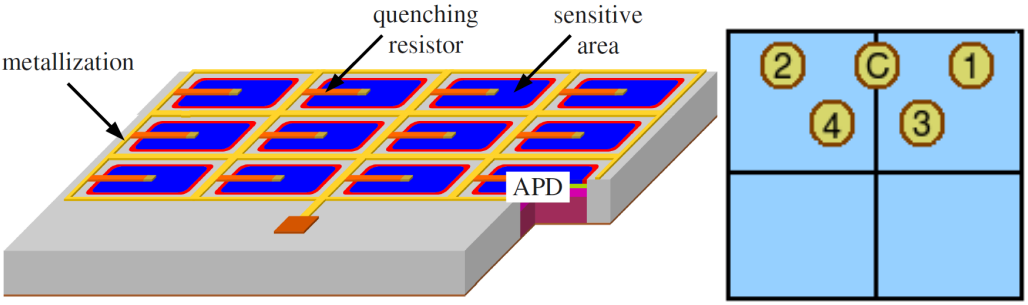

Figure 4.17: The surface of an MPPC consists of 3600 pixel with pixel size of $50 \times 50 mm^2$. Each pixel is connected by metalization to the readout pin (left) [34]. Sketch of the backside of an MPPC array (right). The distance of the metalization layer from pixels to anode is larger for MPPC three and four than for number one and two. Since the metalization has a high internal resistance due to its small size, the measured resistivity of the quenching resistor increases.

The output signal of waveform samples are recorded with a scope using the same setup as used in the dark rate measurement (see figure 4.10). For each MPPC, two waveforms have been analyzed by applying an exponential fit to the falling edge (see figure waveform):

$$A(t) = A_{max} \cdot e^{-\frac{t}{t_c}}$$

where $A(t)$ is the amplitude of the waveform, A_{max} the maximum amplitude and t the time. The results of the time constant of waveform analyses is depicted as a dashed lines in figure 4.18 (left). The solid line describes the results calculated with equation 2.3 using the quenching resistor extracted from the IV-curve and the pixel capacitance from the gain measurement. Both methods are compatible, which means that the gain measurement and IV-curve are reliable, with respect to the model assumption.

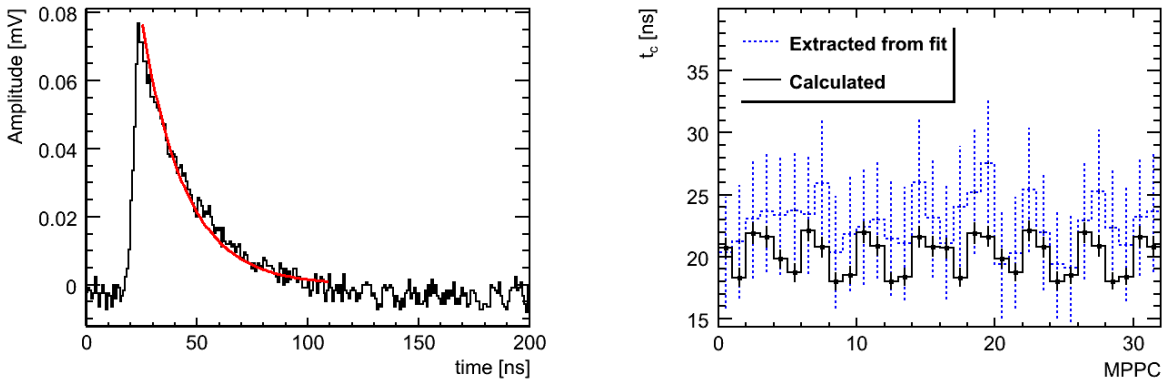

Figure 4.18: Exponential fit on falling edge of waveform recorded with scope (left), time constant t_c extracted from waveform (dashed line) and calculated from gain and IV-curve measurement (solid line) (right).

4.4 Conclusion on MPPC characterization

All 32 MPPCs used in the PET test device have been characterized. The spread of the breakdown voltage and gain (see table 4.1) for the same applied bias voltage is very small with and RMS less than 2 %, which shows a high homogeneity of the MPPCs. The quoted data[11] from the manufacturer have confirmed the results within experimental error, apart from the Dark rate, which has been measured two times larger. A comparison with a measurement where the ADCM is replaced by the QDC shows a lower dark rate which is still out of range to the quoted data, but recently, Hamamatsu has changed their quotation[12] to a higher dark rate which is in agreement with both measurements. A reason for the lower dark rate measured by the QDC could be a different handling of afterpulses. The ADCM measurement sets a threshold on the amplitude and the QDC on the integrated amount of charge. Hence it can occur that in case of the QDC measurement original signal and following afterpulse are falsely counted as one event.

The time constant have been calculated from the positive bias region of the IV-characteristic and the gain measurement. This result is in good agreement with the time constant extracted from an exponential fit on the waveform considering that both results have been derived from three independent measurements. The spread of both measurements is about 10 % RMS.

Properties	Mean	RMS
$G(U = 71\,V)\,[10^5]$	8	0.4
$U_{bd}(T = 25°C)\,[V]$	69.6	0.07
Dark rate $(G = 7.5 \cdot 10^5)$ $[Mcps]$	8.1	0.4
t_c waveform $[ns]$	23.3	2
t_c calculated $[ns]$	19.4	1.5

Table 4.1: Overview table of results of the characterization measurements for all MPPCs. Mean and RMS of the most important properties are quoted. t_c have been extracted from exponential fit on waveform and calculated from gain and IV-curve measurement.

[11] Quoted on the package of each MPPC array (see figure 4.9)
[12] Quotation on the Hamamatsu data sheet for MPPC S103622-33 -50C [3]

Chapter 5

Optimization studies of PET test device

In the following measurements, the PET test device (see section 3) has been used for optimization studies. Both detector modules have a radius of $6\,cm$ to the center where the source ^{22}Na (see section 3.5) is positioned. The emitted positron annihilates with an electron into two back-to-back $511\,keV$ photons which are detected by two opposed detector modules. The threshold is set to $20\,mV$ of the amplitude in order to reject dark rate events. The ADCM is capable of determining coincidences between two channels. Both waveforms are integrated and stored as one event (cf. subsection 3.4.1). The integrated waveforms have been converted into a charge value (see equation 3.1). Figure 5.1 shows the charge distribution for one channel with the Compton edge to the left and the photoelectric peak to the right. Each charge distribution have been analyzed to determine the position of the photoelectric peak. The energy resolution and the number of detected photons of the photoelectric peak are determined in this chapter.

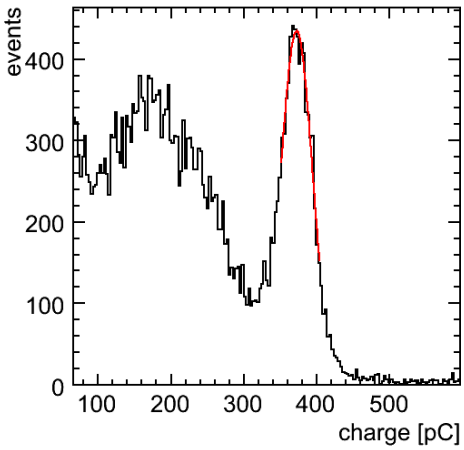

Figure 5.1: Charge distribution of one channel of the PET test device detecting $511\,keV$ photons. A Gaussian fit is applied to the photoelectric peak.

5.1 Optimization of number of detected photons

The number of detected photons N_{det} is the amount of incident photons on the MPPC surface which have been detected by the MPPC. A high number detected photons improves the energy and time resolution. The time resolution $\sigma_t|_{FWHM}$ is the full width half maximum (FWHM) of the distribution of the time difference between two $511\,keV$ photons from the same annihilation, over multiple events. Therefore, it depends on the rise time τ_r and the decay time τ_c of the crystal, as well as the number of detectable N, which is the number of optical photons hitting the MPPC surface. It can be deduced from Shao's equation [35]:

$$I(t) = \frac{N(\tau_c + \tau_r)}{\tau_c^2}(1 - e^{-\frac{t}{t\tau}}) \cdot e^{-\frac{t}{t_c}} \tag{5.1}$$

where $I(t)$ is the intensity of the scintillation light. The exponential terms in equation 5.1 can be replaced by the first order development term, assuming that $\tau_r \ll \tau_c$. This assumption is just valid for the first 5 photoelectrons which determine the timing of the detector and leads to:

$$I(t) = \frac{N(\tau_c + \tau_r)}{\tau_c^2}\left(\frac{t}{\tau_r} - \frac{t^2}{\tau_r \tau_c}\right). \tag{5.2}$$

The integral of the intensity describes the number of detectable photons of the mean arrival time between 0 and t.

$$N(t) = \int_{t'=0}^{t'=t} I(t')dt' = \frac{N(\tau_c + \tau_r)}{\tau_c^2}(\frac{t^2}{2\tau_r} - \frac{t^3}{3\tau_r \tau_c}). \tag{5.3}$$

Rewriting of the second term of equation 5.3 leads to

$$N(t) = \frac{N(\tau_c + \tau_r)t^2}{\tau_c^2 \tau_r}\left(\frac{1}{2} - \frac{t}{\tau_c}\right).$$

For time resolutions below $1\,ns$, the mean arrival time of the first photons t_1 can be assumed to be much smaller than the decay time of LFS, $\tau_c = 40\,ns$ (cf. table 3.1). Hence equation 5.3 can be further simplified to

$$N(t) = \frac{N(\tau_c + \tau_r)t^2}{2\tau_c^2 \tau_r}. \tag{5.4}$$

For the first photon arriving, $N(t_1) = 1$ leads to

$$t_1 = \sqrt{2\tau_c \frac{\tau_r}{N}}. \tag{5.5}$$

Considering that with Poisson distribution the sigma is equal to the mean value, the time resolution amounts to $\sigma_{t,s}|_{FWHM} = 2.35 t_1$. Assuming the same time resolution for two crystals, the coincidence time resolution can be expressed as follows:

$$\sigma_{t,c}|_{FWHM} = 2.35\sqrt{\tau_c \frac{\tau_r}{N}} \tag{5.6}$$

Using this equation, the dependence of the coincidence time resolution on N is depicted in figure 5.2 for two different rise times. The time resolution improves for increasing number of detected photons with a $1/\sqrt{N}$ behavior. The number of detected photons is directly connected to the number of detectable photons by the PDE:

$$N_{det} = PDE \cdot N$$

Therefore, the time resolution improves for a high number of detected photons.

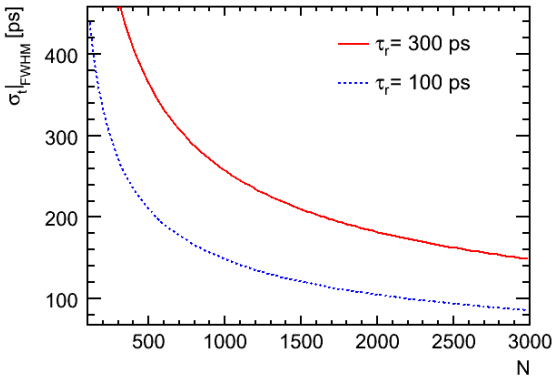

Figure 5.2: Coincidence time resolution according to equation 5.6 as a function of the number of detectable photons. $\sigma_{t,c}|_{FWHM}$ is depicted for $\tau_r = 300\,ps$ (solid line) and $\tau_r = 100\,ps$ (dashed line). $\tau_c = 40\,ns$ have been used.

The number of detected photons can be calculated of the number of fired pixel N_{pix}. For the determination of N_{pix}, the integration range is set to $720\,ns$ in order to integrate the whole waveform of each signal. N_{pix} can be calculated for each event by

$$N_{pix} = \frac{Q}{G(U,T) \cdot e}. \tag{5.7}$$

where Q is the integrated charge of the waveform, $G(U,T)$ (see equation 4.3) the gain and e the elementary charge. The number of detected photons removes afterpulse (AP) and crosstalk (XT) events (see subsection 2.2.3), since those events occur too often to be neglected. Figure 5.3 (left) shows the correlation between crosstalk probability P_{XT} and gain. When one pixel fires, it can produce optical photons, which can trigger an avalanche in a neighboring pixel. Since this process can be repeated several times, the number of fired pixel has to be corrected to

$$N_{pix} = N_{det} \cdot \sum_{n=0}^{N} {P_{XT}}^N.$$

The geometric progression can be solved to

$$\sum_{n=0}^{N} {P_{XT}}^N = \frac{1 - {P_{XT}}^N}{1 - P_{XT}}.$$

For a high number of N, ${P_{XT}}^N$can be neglected. This leads to

$$N_{det} = N_{pix} \cdot (1 - P_{XT}). \tag{5.8}$$

The second effect which also removes fired pixel to N_{det} is afterpulse. Charge carriers generated from an avalanche can be trapped due to crystal impurities. These carriers can be released after a certain time and trigger another avalanche. The probability for afterpulse P_{AP}

increases with increasing voltage over breakdown (cf. figure 5.3 (right)). An exponential and polynomial degree two fit have been performed to extrapolate the curve for higher $\triangle U$. The polynomial degree two fit have been applied for AP corrections, since the chi square divided by the number of degrees of freedom χ^2/ndf is closer to 1 than for the exponential fit. This means, that the deviations of fitted curve to the data points is smaller. The number of fired pixels increases with P_{AP} to

$$N_{pix} = N_{det} \cdot (1 + P_{AP}) \tag{5.9}$$

$N_{det,}$, the number of fired pixel corrected for crosstalk and afterpulse can be derived from equation 5.8 and 5.9:

$$N_{det} = N_{pix} \cdot \frac{1 - P_{XT}}{1 + P_{AP}} \tag{5.10}$$

In the following, N_{pix} and N_{det} are related to the number of fired pixel or detected photons at the mean of the photoelectric peak.

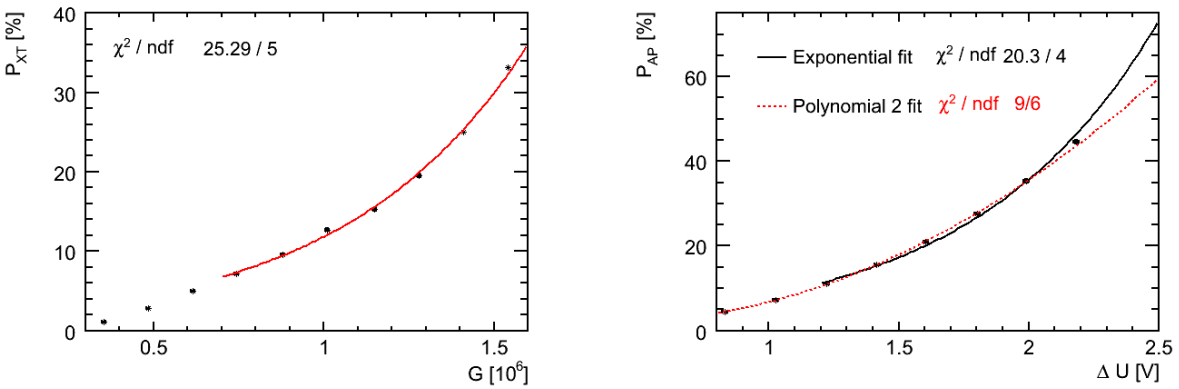

Figure 5.3: Crosstalk probability of a single pixel versus gain. The measurements are fitted by an exponential function (left). Afterpulse probability versus $\triangle U$. The points are fitted by a second degree polynomial and an exponential fit (right). [20]

Figure 5.4 (left) shows N_{det} and N_{pix} versus voltage over breakdown. N_{pix} (solid line) increases considerably stronger with voltage over breakdown than N_{det} (dashed line). This is due to crosstalk and afterpulse events. N_{det} increases due to the PDE dependence on the breakdown voltage (see figure 2.10 (left)). The avalanche probability P_a in equation 2.4 leads to an increase of the PDE (cf. figure 2.10 (left)) and hence N_{det}. Since P_{AP} is out of the range for the last point at $\triangle U = 2.3\,V$ (cf. figure 5.3 (right)), the difference of both fitting curves has been added to the error of N_{det}.

Figure 5.4 (right) shows N_{det} for each channel at $\triangle U = 2.1\,V$. The spread between channels has an RMS of 14.3 % for $\langle N_{det} \rangle = 1219$. The large spread of N_{det} from channel-to-channel arises mainly due to variations in the crystal dimensions and coupling between crystal and MPPC.

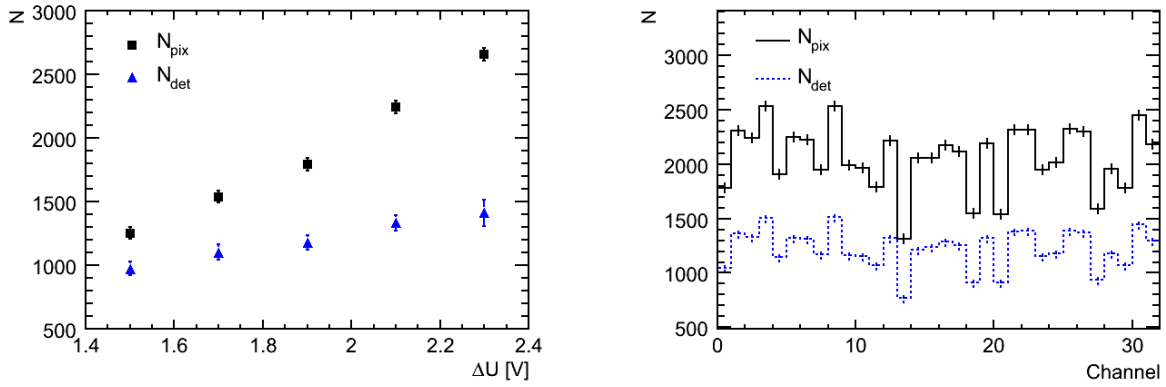

Figure 5.4: Number of fired pixels and number of detected photons depending on $\triangle U$ (left) and for all channels at $\triangle U = 2.1\,V$ (right).

5.2 Optimization of energy resolution

The energy resolution $\frac{\sigma}{E}|_{FWHM}$ indicates how well photoelectric events can be distinguished from Compton events. σ_E can be described by the following formula:

$$\left(\frac{\sigma_E}{E}\right)^2 = \left(\frac{\sigma_S}{E}\right)^2 + \left(\frac{\sigma_I}{E}\right)^2 + \left(\frac{\sigma_N}{E}\right)^2. \tag{5.11}$$

The first term describes the statistical factor of the energy resolution from the fluctuations of the number of detectable photons N. The statistics are Poisson distributed and thus the variance is given by $\sqrt{N}$ and hence $\frac{\sigma_S}{E} \propto \frac{1}{\sqrt{N}}$. This correlation shows that the energy resolution improves for an increasing amount of N, which is proportional to the number of detected photons. This can be achieved with a higher light yield of the crystal and higher PDE of the MPPC in the wavelength region of the emission peak of the scintillator. The second term represents the intrinsic energy resolution of the crystal as described in subsection 2.1.3. The last term comprises the noise contribution from the photodetector and front end electronics.

The energy resolution can be calculated from the charge spectrum (see figure 5.1). The one standard deviation σ_{phe} and the mean Q_{phe} of the photoelectric peak are extracted from a Gaussian fit to this region. $\frac{\sigma}{E}|_{FWHM}$ is obtained scaling the Gaussian σ_{phe} by the factor 2.35:

$$\frac{\sigma}{E}|_{FWHM} = \frac{2.35 \cdot \sigma_{phe}}{Q_{phe}}. \tag{5.12}$$

The left side of the photoelectric peak does not show the expected gap between the Compton edge and the photoelectric peak, which is biased due to multiple Compton scattering events. Therefore, an asymmetric Gaussian fit is performed to exclude this area.

The energy resolution has been investigated concerning the voltage over breakdown, integration range and read out electronics. With rising voltage over breakdown, the PDE increases, but also the dark rate, which has an influence on the third term of equation 5.11. A smaller integration range decreases Q_{phe} but integrates less noise.

5.2.1 Optimization of integration range and $\triangle U$

In the following series of measurements, the energy resolution has been optimized concerning the integration range and voltage over breakdown $\triangle U$. For this purpose, waveforms of one

channel have been integrated for various integration ranges from 120 ns up to 820 ns, which is visualized by the vertical lines in figure 5.5 (left). In figure 5.5 (right) the waveform is normalized to their integral to compare the shape of the waveform for different voltages over breakdown. With rising $\triangle U$ the relative peak height decreases while the tail height increases. The latter effect is due to afterpulses whose probability also increases for higher $\triangle U$(cf. figure 5.3 (right)). The afterpulse probability for $\triangle U = 1.7\,V$ is 24 % and 40 % at $\triangle U = 2.1\,V$. For higher $\triangle U$, afterpulses hence become a significant fraction of the total number of fired pixels. Since an afterpulse is a trapped charge carrier which triggers an avalanche after the recovery time, the ratio between afterpulses and fired pixel from an incident photons is much higher in the tail of the waveform. Because of this, a smaller integration range would exclude fired pixel due to an incident photon and a large portion of afterpulses.

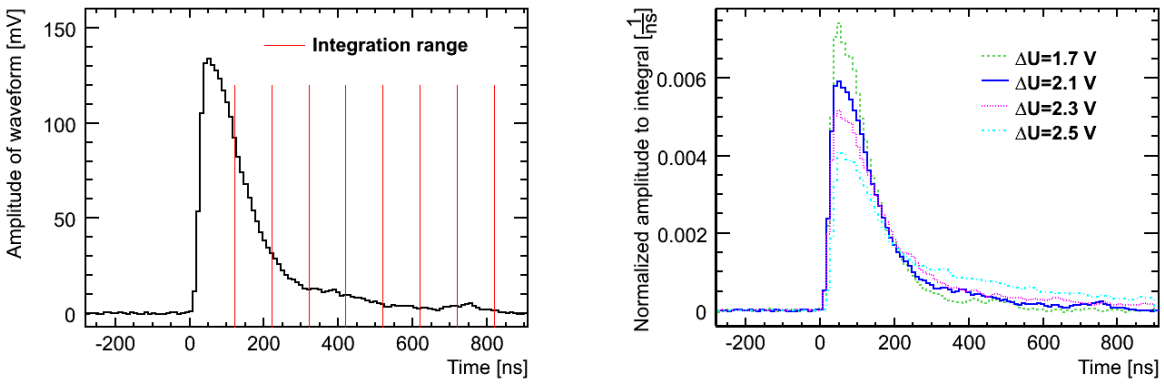

Figure 5.5: Waveform of photoelectric event for $\triangle U = 2.1\,V$. The vertical line illustrates the integration limit (left). Waveforms for different voltages over breakdown (right). Each waveform has been normalized to their integral to investigate the dependence of $\triangle U$ on the shape of the waveform.

A small integration range can compensate the disadvantage of a high voltage over breakdown, which increases the PDE, but also generates more noise. Therefore, the energy resolution improves with increasing $\triangle U$ and decreasing integration range. For a too high $\triangle U$ and integration range, the dark rate and P_{AP} becomes significant high and the principal part of the waveform is not covered anymore. Hence the energy resolution worsens again (cf. figure 5.6(left)). The best relative energy resolution is reached for an integration range around 200 ns, when only the principal part of the signal is integrated for a preferably high $\triangle U$. The best result for 420 ns delivers the highest $\triangle U = 2.5\,V$, which causes a high dark rate with an afterpulse probability already higher than 50 %. As a consequence the best reliable result is achieved for $\triangle U = 2.1\,V$ at an integration range of 220ns. Figure 5.6 (right) shows a comparison of this result to an integration range of 720 ns and $\triangle U = 1.7\,V$. The mean energy resolution amounts to $\frac{\sigma}{E}|_{FWHM} = 16.3 \pm 1.3\,\%$ which is 11 % worse than $\frac{\sigma}{E}|_{FWHM} = 14.7 \pm 1.6\,\%$ for the chosen combination of integration range and $\triangle U$. Measurements with two channel systems have achieved $\frac{\sigma}{E}|_{FWHM} = 11\,\%$ for crystals wrapped in Teflon [6]. The crystals used in the PET test device are comprised of aluminum, which has a reflectivity about 20 % lower than that of Teflon, which decreases the light yield of the crystals [37]. Since the number of fired pixels decreases linearly with the light yield, the energy resolution is expected to be lower because of the first term in equation 5.11.

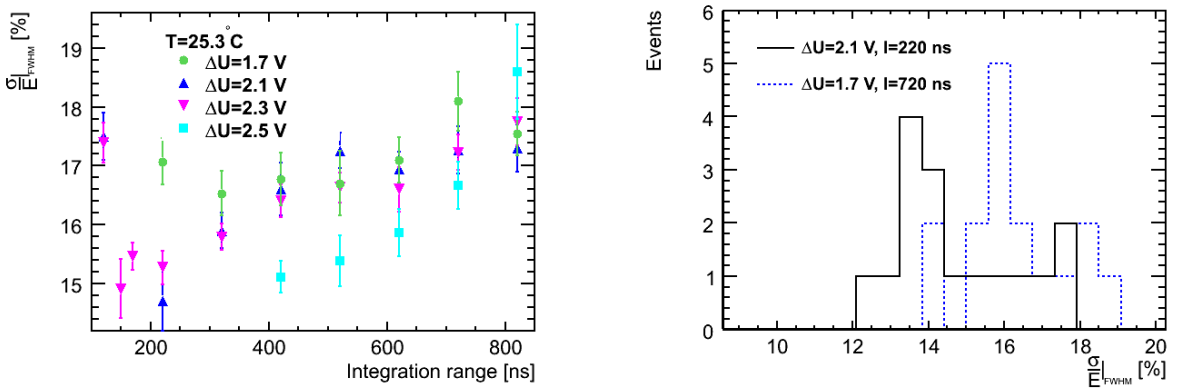

Figure 5.6: Energy resolution $\frac{\sigma}{E}|_{FWHM}$ versus integration range for four different over voltages for one channel (left). The distribution of the energy resolution for $\triangle U = 1.7\,V$ and an integration range $I = 720\,ns$ is 11 % worse than for the optimized combination of $\triangle U = 2.1\,V$ and $I = 220\,ns$ (right).

5.2.2 Comparison of data acquisition with ADCM and QDC

The resolution and the contribution of noise of the DAQ module influence the energy resolution. This subsection investigates if a different choice of front end electronics have an impact on the energy resolution. Therefore, the same signals have been recorded by the ADCM and QDC using the setup described in figure 5.7 (left). Two crystals are positioned on opposite sides in a light-tight box. One channel is used as a trigger while the data of the other channel is recorded by ADCM and QDC. A fan-in and fan-out is a device which splits a signal and doubles its amplitude. Thus two devices are used to split the signal of both channels to ensure that the same signals are recorded by both front end electronics. In case of measuring with the QDC, the trigger signal is discriminated and the gate generator is used to set an integration range of $320\,ns$. The same gate is set in the DAQ software of the ADCM. The results in terms of energy resolution $\frac{\sigma}{E}|_{FWHM}$ are depicted in figure 5.7 (right). Two MPPCs have been investigated for U=71.4 and U=71.8 V. For each measurement, the $\frac{\sigma}{E}|_{FWHM}$ is smaller in the QDC, especially for the higher bias voltage. The difference of $\frac{\sigma}{E}|_{FWHM}$ for each measurements leads to a mean value of (1.9 ± 1.3) % points. Reasons for the inferior energy resolution measured by the ADCM can be the resolution, the contribution of noise or the digitization and conversion. The QDC converts voltage pulses in a digitized number of charge while the ADCM measures the output charge of one pulse by summing up the samples (cf. subsection 3.4.2). But the sensitivity of the ADCM of $20\,fC/ch$ is higher than the QDC $50\,fC/ch$ and thus cannot explain the difference of the energy resolution. The contribution of noise is another feature of a DAQ module. The dark rate measurement has shown a dark rate which is about $1\,Mcps$ higher than measured by the QDC (see 4.2.2). But the amount of electronic noise is negligible small in comparison to the dark rate (see figure 4.11(left)). Hence the reason for deviation of both results might be the digitization and conversion of the signal. Further studies are required to confirm this assumption.

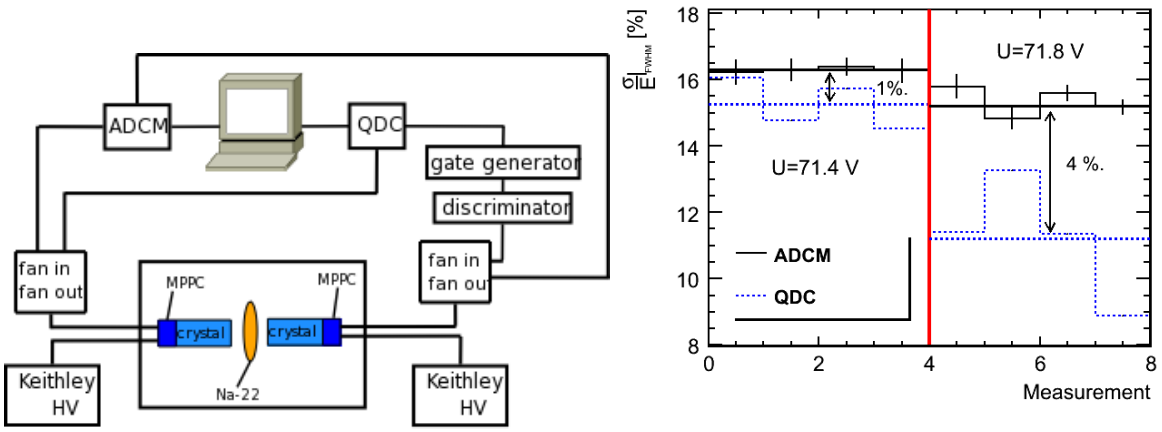

Figure 5.7: Setup of two channel coincidence measurement using fan-in fan-out to compare DAQ of same waveforms with ADCM and QDC (left). Comparison of $\frac{\sigma}{E}|_{FWHM}$ measured with QDC (dashed line) and ADCM (solid line) using two different MPPCs (right). The first four measurements have been performed for $U = 71.4\,V$ leading two an average difference of the energy resolution of 1 % point. The subsequent measurements for $U = 71.8\,V$ resulted in an average difference of 4 % points.

5.3 Optimization of the MPPC voltage working point

The MPPC characterization measurements of the previous chapter is used here to optimize the system with respect to different read out options. By applying a certain bias voltage for each channel, the system can either be adjusted to the same mean of the photoelectric peak or the same gain. Both optimization points change with temperature fluctuations, which can also be compensated by voltage adjustment. Each method has advantages and disadvantages and will be investigated concerning energy resolution, number of detected photons and dark rate. A discussion of each method should lead to a determination of the best suited method for each experiment.

5.3.1 Method 1: Voltage adjustment to same mean of photoelectric peak

The adjustment of the mean to the same value is important when the Compton rejection threshold is applied from hardware and is the same for each channel. The discrimination of the Compton events with a common discriminator level reduces the amount of data transfer at a a very moderate investment in electronics.

The position of the mean of the photoelectric peak depends on the gain and on the PDE of the MPPC which both depend on the temperature and bias voltage of the MPPC (cf. equation 4.3). Differences between the channels arise mainly due to variations in the crystal dimensions and in the coupling to the sensors. This can be compensated by voltage adjustments with the HV module, which allows to set the bias voltage for each channel individually in order to get the mean of the photoelectric peak to the same value. The accuracy of the HV module is limited to $36.3\,mV/ADU$ (cf. subsection 3.3.1), which leads to a spread of RMS of $6\,pC$ from the mean value of $384\,pC$ (see figure 5.8 (left)). The spread of $\triangle U$ from channel-to-channel is between 1.9 and $2.6\,V$ which is a rather high. This leads to large differences in crosstalk and afterpulse. As an example the afterpulse probability which roughly doubles from $\triangle U = 2.1\,V$ to $\triangle U = 2.6\,V$.

5.3.2 Method 2: Voltage adjustment to same gain

When the system is adjusted to the same gain, a single photon generates the same amount of charge carriers in each MPPC. Consequently, the waveform amplitude of a single-photon is equal for each MPPC, if the waveform shape is also the same. The determination of the time constant by two different methods have shown the same time characteristic for all MPPCs (cf. section 4.3). By setting a threshold below the maximum amplitude of the waveform, it is possible to trigger the system upon the first photon detected. Since the same threshold can be applied for each channel, this method is suited for time resolution measurements. As depicted in the dashed line in figure 5.8 (left), the differences of $\triangle U$ from channel-to-channel for a $G = 12 \cdot 10^5$ are within error. From this point of view, the same conditions for crosstalk and afterpulse can be assumed for each channel.

A disadvantage is the large channel-to-channel deviation for the position of the photoelectric peak (see dashed line in figure5.8 (right)) which makes it impossible to set a common Compton rejection threshold. The mean results to $355\,pC$ with a RMS of $13\,\%$.

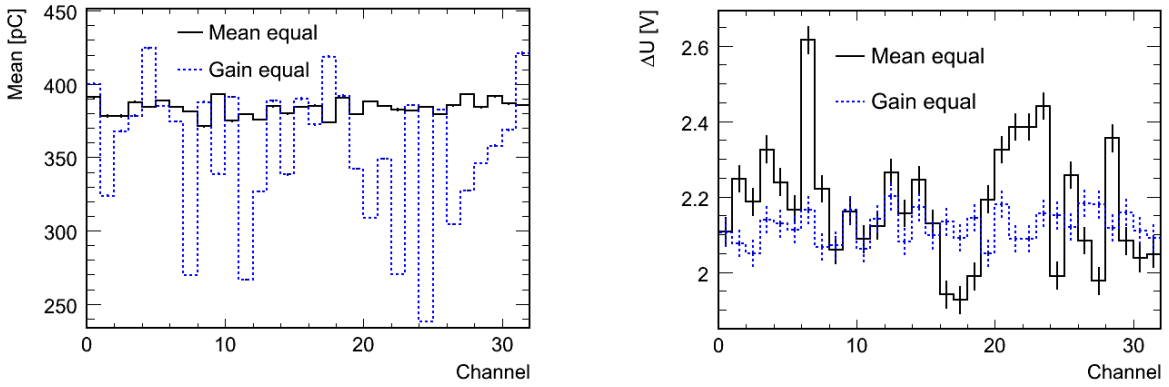

Figure 5.8: Mean of the photoelectric peak (left) and $\triangle U$ for $G = 12 \cdot 10^5$(right) of each channel for method 1 (solid line) and method 2 (dashed line).

5.3.3 Compensation of temperature changes

When the MPPC working point is adjusted to a certain readout option, it is imperative to reach long term stability concerning the gain or position of photoelectric peak. For long term measurements, large temperature fluctuations can occur. Since the breakdown voltage increases linearly with temperature by $a_T = 56\,mV/K$ (see subsection 4.1.3), the gain and hence the position of the photoelectric peak changes. Therefore, the bias voltage U(T) has to be adjusted to keep the voltage over breakdown $\triangle U = U(T) - U_{bd}(T)$ constant using equation

$$U'(T') = U(T) + a_T \cdot (T' - T). \tag{5.13}$$

The breakdown voltage changes linearly with $\triangle T = T' - T$ with gradient a_T (cf. figure 4.6 (right)). By adjusting the bias voltage U' for the change of the breakdown voltage $\triangle U_{bd} = a_T \cdot \triangle T$, the voltage over breakdown can kept constant, which also leads to a constant gain. Hence the dark rate, the PDE crosstalk probability, afterpulse probability and the position of the photoelectric peak won't change either. Figure 5.9 shows the position of the photoelectric peak measured for various temperatures with voltage adjustments. The method is limited by the accuracy of the HV, which adjust the voltage in ADU steps (cf. subsection 3.3.1). One ADU step corresponds to $36.3\,mV$ in average and a temperature change of approximately $0.6\,°C$.

Because of this, the position of the photoelectric peak can be kept constant in a range around $20\,pC$.

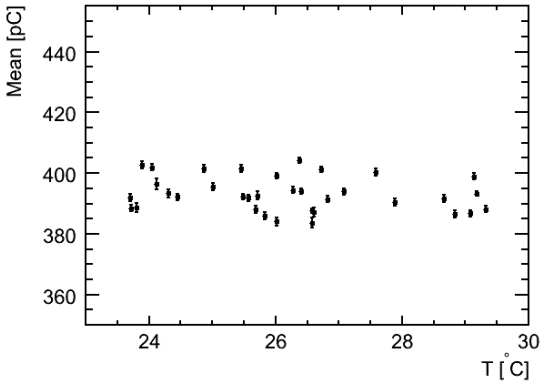

Figure 5.9: Mean of the photoelectric peak versus temperature for different measurements. For each measurement, the voltage has been adjusted to compensate a shift of the photoelectric peak due to temperature changes.

5.3.4 Comparison of both methods

Energy resolution, number of detected photons and the dark rate are further important properties that describe the performance of the detector. A comparison of these properties may lead to further statements about advantages and disadvantages of the respective method.

The energy resolution is depicted in figure 5.10 (left) and the number of detected photons in figure 5.10 (right). Mean and RMS of both methods are listed in table 5.1 and show no significant differences, neither for $\frac{\sigma}{E}\,|_{FWHM}$ nor for number of detected photons. The same result for the dark rate which is depicted in figure 5.11 for both methods.

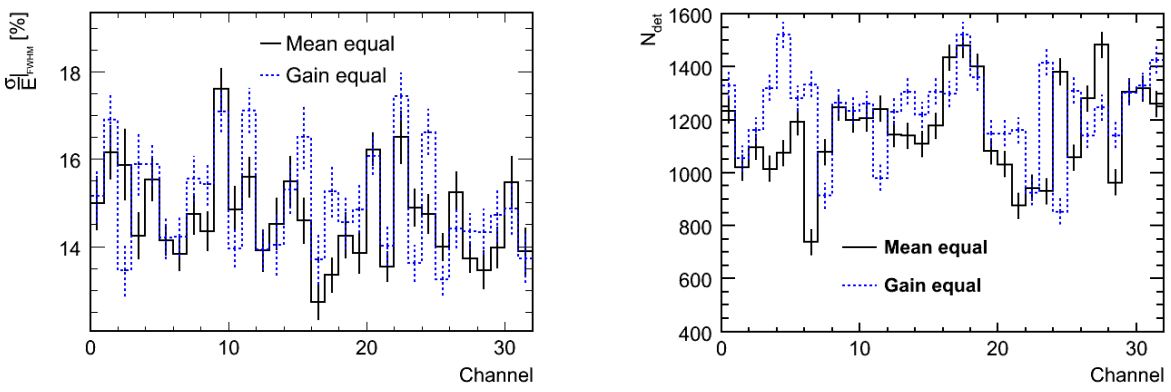

Figure 5.10: Energy resolution (left) and number of detected photons (right) of each channel for the voltage working point optimization according to method 1 (solid line) and method 2 (dashed line).

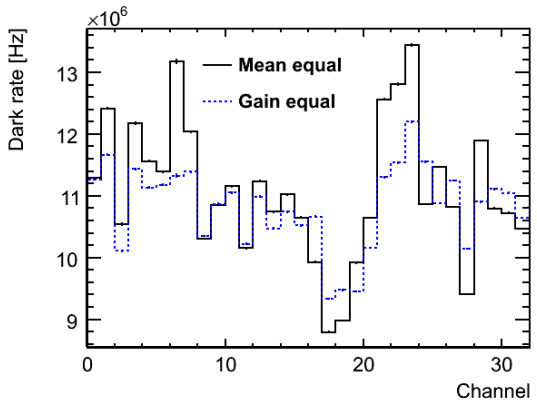

Figure 5.11: Dark rate of each channel for the voltage working point optimization according to method 1 (solid line) and method 2 (dashed line).

Property		method 1	method 2
ΔU	Range [V]	1.9-2.4	2.05-2.2
Gain	Range [10^5]	11-14	12
Mean of photoelectric peak	Mean [pC]	384	364
	spread [pC]	3	30
$\frac{\sigma}{E}\mid_{FWHM}$	Mean [%]	14.7	14.8
	RMS [%]	1.1	1.3
N_{det}	Mean	1160	1213
	RMS	175	144
Dark rate	Mean [Mcps]	11.1	10.8
	RMS [Mcps]	1.1	0.7

Table 5.1: Summary table of characteristic properties for the voltage working point optimization according to method 1 and method 2

5.4 Conclusion on the voltage adjustment method

Two voltage adjustment methods have been tested. Method 1 allows to reduce the data rate from a multichannel system by applying a common discrimination threshold to all channels. For this, the response to photoelectric events is equalized and the threshold can be adjusted to remove all or partially the Compton events. The voltage adjustment leads to a spread of the gain and voltage over breakdown and hence for the PDE, afterpulse and crosstalk probability.

Method 2 equalizes the MPPC gain and, given the small spread in signal shape among the MPPCs, also the amplitude of a single-photon signal. In this way, precise measurements of time resolution can be performed where the timing threshold is fixed to 0.5 photoelectron amplitude. Since the gain is equal, the voltage over breakdown is also constant within error. Therefore, each channel has the same conditions for crosstalk, afterpulse and PDE. A compensation for temperature changes keeps $\triangle U$ and its related properties constant within a range determined by the accuracy of the HV module. Various observables have been compared for both adjustment methods (see table 5.1) with no significant advantage for each of them.

The optimization studies of the energy resolution resulted with an integration range of $220\,ns$ and a voltage over breakdown of $\triangle U = 2.1\,V$. Hence both methods have been operated

around this voltage over breakdown. A comparison of ADCM have shown an improvement of the energy resolution for a mean value of 2 % points for the QDC. A reason for the worse energy resolution measured by the ADCM might be the digitization and conversion of the signal, but have to be further investigated.

The number of fired pixel have been integrated for an integration range of $720\,ns$ in order to cover the whole signal. By removing afterpulse and crosstalk events, the number of detected photons can be calculated. Large deviations of channel-to-channel have been observed, which are due to different crystal sizes and their coupling to the MPPCs.

Chapter 6

Spatial resolution of the detector

The spatial resolution $\sigma_r|_{FWHM}$is a characteristic parameter to describe the performance of a detector, as it shows how well an image can be resolved. The resolution is limited by the positron range, non-collinearity and intrinsic resolution (see chapter 1.1). The emitted positron from ^{18}F has a kinetic energy of $122\,keV$ which leads to a mean positron range of $R_{mean} = 0.6\,mm$ (see table 1.1). Figure 6.1 (left) shows the dependence of R_{mean} on the kinetic energy of common radionuclides used in PET. For a rough estimation of R_{mean} for ^{22}Na, a linear behavior can be assumed. The emitted positron of the ^{22}Na source has a kinetic energy of $33\,keV$ (see section 3.5), hence $R_{mean} \approx 0.14\,mm$.

The non-collinearity effect (see figure 6.1 (right)) increases the spatial resolution with radius R to the detector module. The error due to non-collinearity, can be calculated to

$$\sigma_{nc}|_{FWHM} = 0.0044 \cdot R \tag{6.1}$$

where R is the radius of the detector ring in mm [38]. Since the interaction point of the incident photon in the crystal is unknown, the detector width has a major impact on the spatial resolution. For example, a channel size of 4x4 mm^2 limits the spatial resolution to about 2 to 3 mm [10]. Theoretically, the detector sensitivity to lines of response is maximum at the center and falls of to zero at the edges. This sensitivity modeled as a triangular response function has a FWHM at half the detector size [39]. This assumption is just valid, when the source is positioned in the center. Since crystal and MPPC width are $w_c = 3\,mm$, the intrinsic spatial resolution can be estimated to 1.5 mm. Summarizing all, the spatial resolution of the PET detector can be estimated as:

$$\sigma_r|_{FWHM} \approx \sqrt{(0.0044 \cdot R)^2 + \left(\frac{w_c}{2}\right)^2 + (R_{mean})^2}. \tag{6.2}$$

Assuming a source of ^{22}Na with zero extension, $\sigma_r|_{FWHM} \approx 1.57\,mm$ can be expected as a lower limit for R=10 cm.

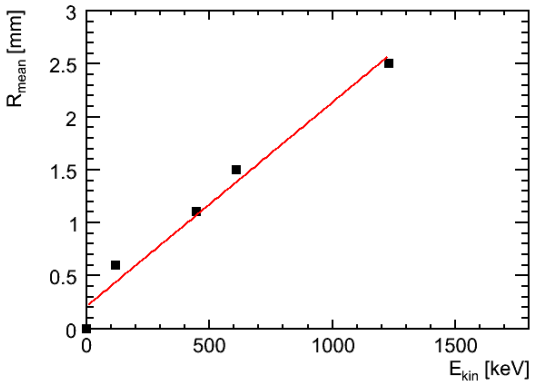

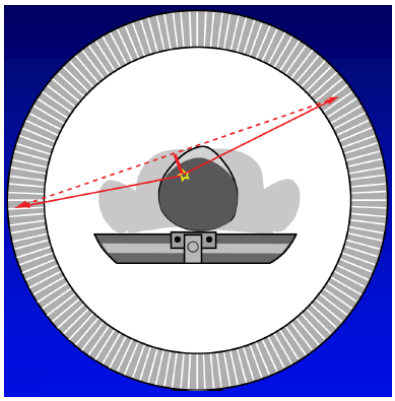

Figure 6.1: R_{mean} versus E_{kin} of common radioactive nuclides used in PET (see table1.1) (left), Illustration of the non-collinearity effect (right) [38].

6.1 Scan of two ^{22}Na sources

The PET test device described in chapter 3 is used for the following measurements. A compound of two point-like ^{22}Na sources with a distance of 10 mm are positioned in the center of the setup. From two photoelectric events, a LOR can be derived given by the positions of the crystal center. In order to detect all possible LOR, the detector modules have to be rotated around its center. The field of view (FOV) describes the area which can be covered by the detector modules. A complete scan of the source has four parameters (see figure 6.2):

- R: Radius of detector module.
- N: Number of angular steps.
- α : Size of angular steps in degrees. The total angle $\phi = \alpha \cdot N < 180°$, because of the detector symmetry.
- β: Angle deviation between both modules to increase the FOV. The original setting is $\beta = 0°$ for both detector modules on opposed side.

In order to scan the source from all directions, the detector modules can either rotate around the center or the rotation table in the center rotates, on which the source is positioned (see figure 3.1 (right)). In the following measurements the latter option have been chosen using a rotation stage, which is steered by a computer. A complete scan has to prepared as follows: The radius of the modules have to be adjusted manually. Depending on R, the angles β, α and hence $N = 180°/\alpha$ have to be chosen such that large gaps in the angular acceptance as well as overlapping of LOR are avoided which would deteriorate the image quality. The data taking time t_d has to be increased for larger R, since the intensity of the source decreases with $1/R^2$.

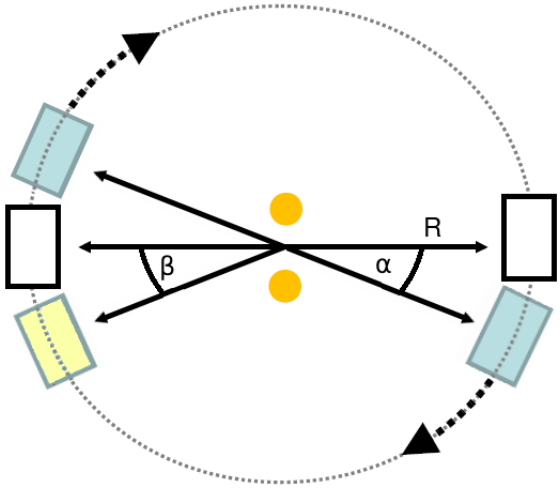

Figure 6.2: Sketch of the parameters which are important for a scan of the ^{22}Na source. Both detector modules oppose each other with a radius R. To perform a complete scan of the source, both modules are rotated by an angle α. It is also possible to rotate just one detector module by an angle β.

The initial settings N, α and t_d have to be typed in a bash script[1]. Afterwards, the scan is steered by the same computer, which steers the rotation stage. The voltage working point is optimized to method 1 (see subsection 5.3.1) in order to set the mean of the photoelectric peak to the same position. Between each angular step the program adjusts the voltage to compensate temperature changes (see subsection 5.3.3). In the following, the results of a scan with 12 angular steps of $\alpha = 15°$, at $R = 11\,cm$, will be presented. A data taking time of $t_d = 10\,min$ have been chosen in order to acquire a sufficient amount of data. The source has been positioned in the center of the top part of both detector modules. The ADCM records the channel output and determines coincidences between both modules. The two channel IDs and the two integrals of the waveforms are stored as one event. The recorded data of each scan are analyzed by a C++ program which converts the integral into a charge value and samples them corresponding to their channel ID. Figure 4.13 shows the charge spectrum for each channel of the top part of module 1 and 2 for the first angular step at $\phi = 0°$. It also shows the position of each channel with respect to the approximate position of the two sodium sources. The positions of the photoelectric peaks in the charge spectra are are equal within a small range. In order to select photoelectric events, Compton events are rejected by an energy cut at 320 pC. The cross hatched area in the photoelectric peak shows the fraction of true coincidence events. Note, that both coincidence events have to be photoelectric events.

[1] A bash is a command processor which reads Linux commands from a text file and executes them

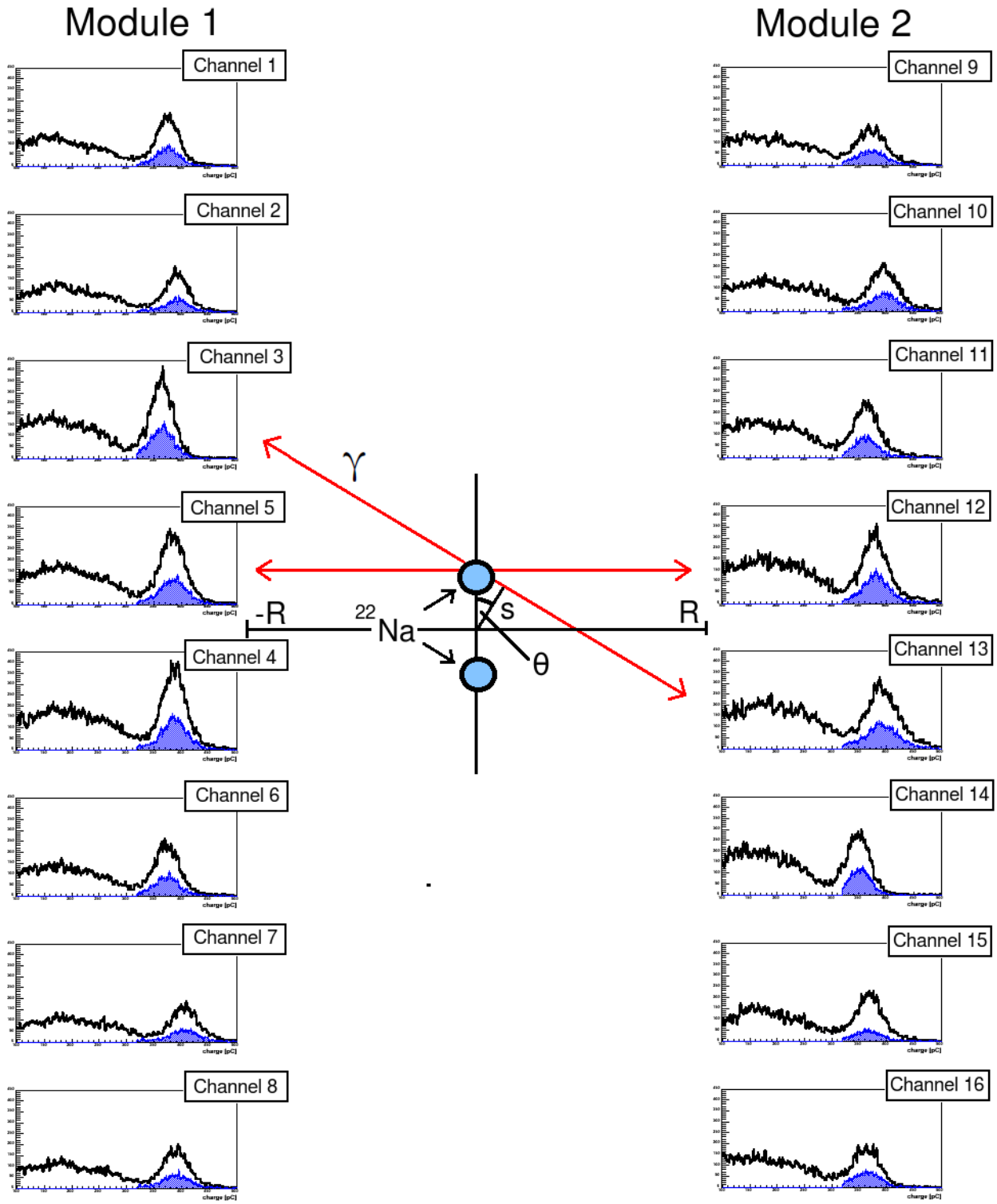

Figure 6.3: Charge spectrum of top layer of module 1 and module 2 with radius $R = 11\,cm$ and $\phi = 0°$. The x-axis shows the integrated charge from $100\,pC$ to $600\,pC$ and the y-axis the amount of events up to 450. The cross hatched area in the photoelectric peak shows the fraction of true coincidence events. The arrangement of spectra and both sodium sources illustrates the experimental setup. For each coincidences a LOR of response can be derived described by the angle θ and the smallest distance of approach s.

For the complete scan, the mean rate of all events, Compton events, photoelectric events and true coincidences of each channel are depicted in figure 6.4 (left). The rate of the bottom part of both modules is about 30 % lower than the top part, which shows that the source is approximately in the same plain as the bottom part of both modules. The fraction of the rate of true coincidences is even lower and amounts to 5 %. The small rate of $0.2\,cps$ contributes too small amount of true coincidence events to derive a reliable image. Hence, in the following only the top part of both modules will be considered.

Figure 6.4 (left) also shows a higher rate of the MPPCs positioned in the center, which is in agreement with the position of the ^{22}Na source (see figure 6.3). The total rate of module 2 is higher which is is due to the trigger logic of the ADCM (see subsection 3.4.1). A coincidence time window opens when a signal triggers an event in module one. All events in module two within this time window are recorded. Therefore, the amount of total events is higher in module 2. Note, that this doesn't effect the rate of true coincidences.

Figure 6.4 (right) shows the rate for each angular, which is expressed as ϕ. The rate increases until it reaches a maximum at the position where both sources are aligned. In this case both points sources are centered and hence more LOR are possible between both detector modules. The total coincidence rate CR of the top part of both modules includes the rate of each angular step and amounts to $CR = 5.7\,kcps$. In this case the detector elements covers a surface of $S = 16 w_c^2 N = 17.3\,cm^2$, where w_c corresponds to the crystal width and 16 to the amount of channels. This is a fraction of 83.4% of the total ring-surface $S_t = 2\pi R w_c$ at $R = 11\,cm$. The source had an activity $A_0 = 1\,MBq$ between two and three years ago. Today's activity can be calculated using

$$A(t) = A_0 e^{-\frac{ln2}{\tau_{1/2}} t} \tag{6.3}$$

with $\tau_{1/2} = 2.6\,a$ being the half life of ^{22}Na (see section 3.5). ^{22}Na decays to 10 % via gamma decay and 90 % via β^+ decay. Since each positron decays into two $511\,keV$, the relation between $A(t)$ and the amount of generated photons is $A_\gamma(t) = (2 \cdot 0.9 + 0.1) A(t)$. The intensity at $R = 11\,cm$ can be calculated by dividing $A_\gamma(t)$ by the spherical surface:

$$I(t) = \frac{1.9 A_0}{4\pi R^2} e^{-\frac{ln2}{\tau_{1/2}} t} \tag{6.4}$$

The interaction probability of a photon in the crystal can be calculated to

$$P = 1 - e^{-\frac{l}{\lambda}}$$

with $l = 1.5\,cm$ being the length of the crystal and $\lambda = 1.12\,cm$ the attenuation length of LFS (cf. table 3.1). When $P = 0.74$, the probability for a coincidence is $P_c = P^2 = 0.55$. Multiplying equation 6.4 by P_c and the covered surface S, gives a rough estimation of the expected total rate of one detector ring:

$$CR_{theo} = \frac{A_0 P_c S}{4\pi R^2} e^{-\frac{ln2}{\tau_{1/2}} t}. \tag{6.5}$$

Assuming $t = (2.5 \pm 0.3)$ and an uncertainty for the photon interaction in the crystal of 5 %, equation 6.5 results to $CR_{theo} = (6.1 \pm 0.4) kcps$, which is within error with the measured rate $CR = 5.7\,kcps$. With this value the amount of true coincidences can be calculated.

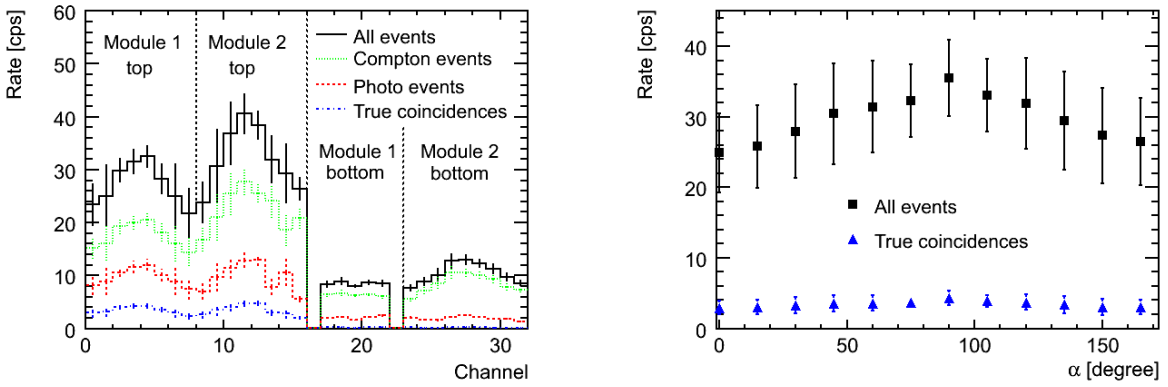

Figure 6.4: Mean rate of each channel of all angular steps (left). Fraction of photoelectric and Compton events of the first 16 channels of all angular steps. The error is the RMS derived from all angular steps.

The fraction of photoelectric events is (33±5) % and (67±5) % for Compton events (see figure 6.5). This leads to a true coincidence fraction of 10 % and hence a rate of $CR_{true} = 0.57\,kcps$.

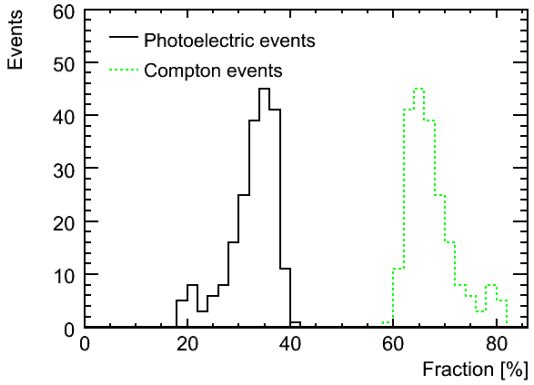

Figure 6.5: Fraction of photoelectric and Compton events of the first 16 channels of all angular steps.

Only true coincidences contribute for image reconstruction. The coordinates of both detector elements are assumed to lay in the center of the corresponding crystal. From both points, a LOR is derived. All LOR are sampled in a sinogram after applied radon transformation (see section 1.2). The sinogram of two ^{22}Na point sources is depicted in figure 6.6, where each colored pixel corresponds to a certain LOR. The amount of LOR in one pixel is illustrated by the color palette to the right. Due to the detector geometry all sampled LOR from one angular are diamond-shaped. The diamonds in the sinogram correspond to N=12 angular steps of $\alpha = 15°$. The white pixels in between are due to small gaps between the crystals, while the area covered by the diamonds determines the field of view. The gaps between the diamonds and pixels are referred to as acceptance gaps. The backprojection from this sinogram leads to a blurred reconstructed image (see figure 6.6 (right). A star-like artifact is recognizable which is due to the summation of all LOR in the center.

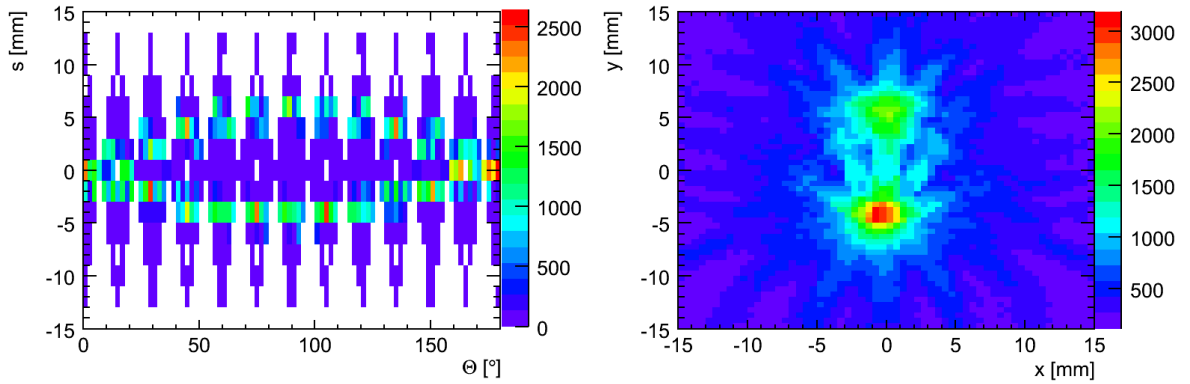

Figure 6.6: Sinogram (left) and reconstructed image (right) of two ^{22}Na point sources for $R = 110\,mm$, using BP (right).

To avoid the effect of $1/r$ blurring (see section 1.2), the filtered backprojection method is applied. For this purpose the inverse 2D Fourier transform is used to apply a ramp filter which amplifies high-frequencies in the frequency domain. The filtered sinogram (see figure 6.7 (left)) is backprojected which reduces the blurring in the image (see figure 6.7 (right)). The bottom source point (SP1) and the top source point (SP2) are well separated.

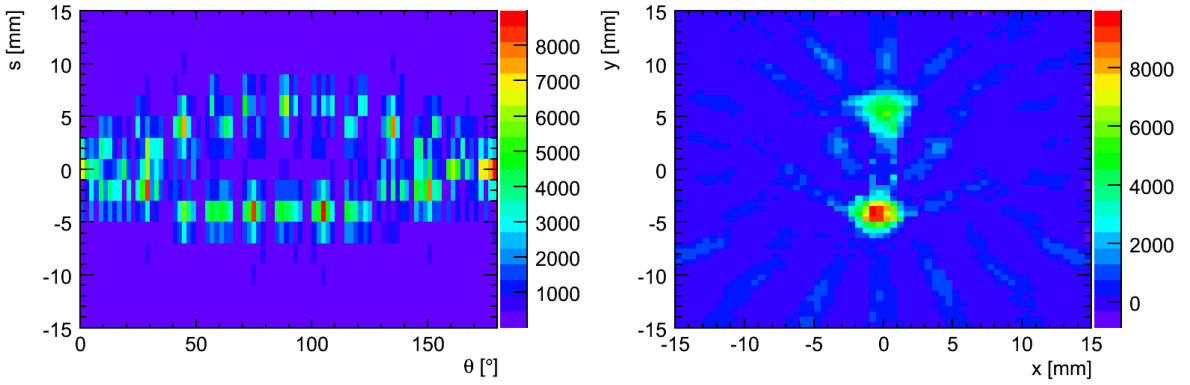

Figure 6.7: Sinogram (left) and reconstructed image (right) of two ^{22}Na point sources for R=165 mm, using FBP (right).

Figure 6.8 shows the x-projection (left) from $y = -10\,mm$ to $y = 0\,mm$ and the y-projection from $x = -5\,mm$ to $x = 5\,mm$ (right) of the reconstructed image by FBP. Adding the projection from $y = 0\,mm$ to $y = 10\,mm$, the coordinates, $\sigma_r|_{FWHM}$ and integral of both source points can be determined (see table 6.1). The spatial resolution$\sigma_r|_{FWHM}$ is the FWHM extracted from a Gaussian fit on the x and y-projections and amounts to $2.4\,mm$, except a worse resolution of SP1 in y-direction, which is also recognizable in figure 6.8 (right). This is caused by the lower activity of SP2, which has approximately 20 % less activity[2] than SP1. Due to its higher activity, the LORs of SP1 overlap SP2 and hence amplifies blurring of SP1 in y-direction. The relative positions of both source points have been determined from the coordinates to 9.85 mm which is in good agreement with the expected distance of 10 mm.

[2]The fraction of the activity have been derived from the integral of both source points on the y-projection.

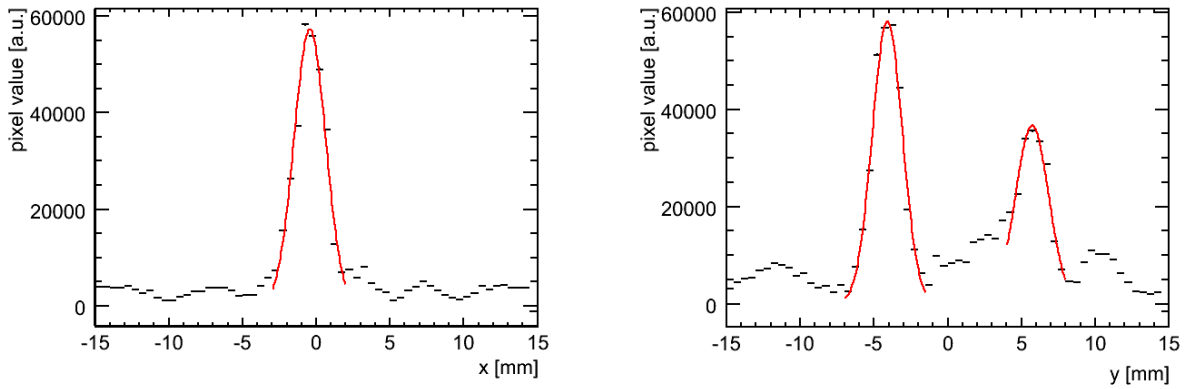

Figure 6.8: X-projection from $y = -10\,mm$ to $y = 0\,mm$ of the reconstructed image (left) and y-projection from $x = -10$ to $x = 10\,mm$ (right).

	x1	y1	x2	y2
coordinates $[mm]$	-0.43	-4.12	0.16	5.78
$\sigma_r\|_{FWHM}$ $[mm]$	2.44	2.35	2.35	2.72
Integral $[10^5]$		4.2		3.5

Table 6.1: Coordinates of SP1: (x_1,y_1) and SP2: (x_2,y_2), as well as $\sigma_r|_{FWHM}$ and integral of both source points. The results have been derived from x and y-projections on the image.

Applying a cut on the pixel value at 2000 leads to a further improvement of the image (see figure 6.9 (left)). The 3D image shows, that both source points are well resolved (see figure 6.9 (left)). Hence a pixel value cut off at 1000 have been applied for the following studies of the spatial resolution dependence on the detector radius.

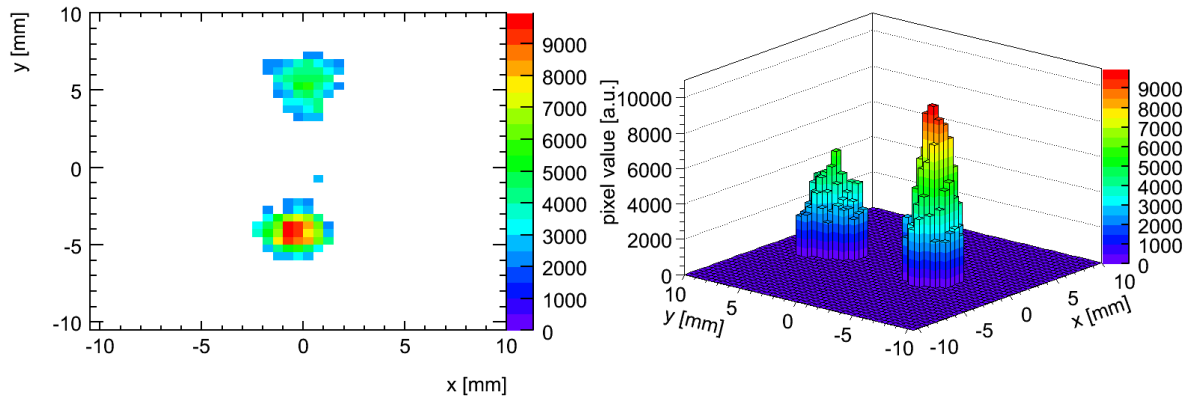

Figure 6.9: Reconstructed image with cut at pixel value smaller than 2000 (left) and 3D view.

6.2 Scan of detector radius

In order to investigate the dependence on the spatial resolution $\sigma_r|_{FWHM}$ on the radius, scans of the source have been performed for five different radii. The initial settings of each scan are listed in table 6.2. The mean rate of each scan depending on the radius is depicted in figure

6.10 (left). Since the intensity of source decreases with $1/R^2$, a fit of this function have been performed on the data points. The expected behavior have been confirmed within error.

$R\,[cm]$	8	11	14	16.5	18.5
$t_d\,[min]$	5	10	20	25	30
$\alpha\,[°]$	20	15	12	10	9
N	9	12	15	18	20

Table 6.2: Data taking time t_d, angle α and angular step N adjusted to the radius R of the modules.

The spatial resolution has only been determined for SP1 with a pixel value cut at 1000. $\sigma_r|_{FWHM}$ shows no correlation to R and remains constant within error. The spatial resolution of the y-projection $\sigma_y|_{FWHM} = (2.1 \pm 0.1)\,mm$, is 10 % smaller than of the x-direction $\sigma_x|_{FWHM} = (2.3 \pm 0.1)\,mm$. The mean resolution of the detector amounts to $\sigma_r|_{FWHM} = (2.2 \pm 0.2)\,mm$. The theoretical spatial resolution (cf. equation 6.2) can be calculated to $1.71\,mm$ for $R = 18.5$ and to $1.54\,mm$ for $R = 8\,cm$, which is about 35 % superior to the measured value. Note, that the theoretical value has just been a rough estimation with the assumption of zero extension of the ^{22}Na source.

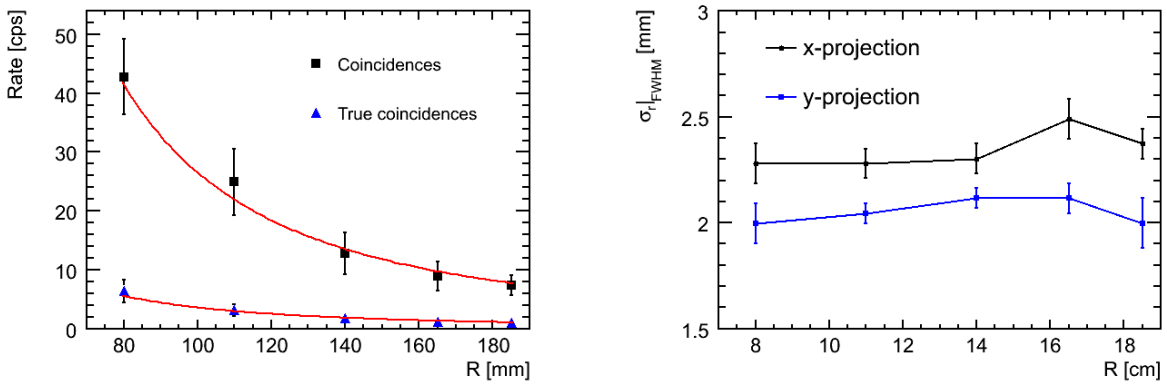

Figure 6.10: Rate of all channels for $\phi = 0$ versus R (left). Spatial resolution for x-projection (triangle) and y-projection (block) versus R (right).

The spatial resolution decreases for larger R due to the non-collinearity effect by 0.2 mm, but the angular coverage improves. Figure 6.11 shows a comparison of a sinogram for $R = 8\,cm$ and $R = 18.5\,cm$. To illustrate the angular coverage just the part of both sinograms for $s < 0$ and θ, ranging from 60° to 120°, is depicted. The acceptance gaps for $R = 8\,cm$ are distinct larger than for the largest radius.

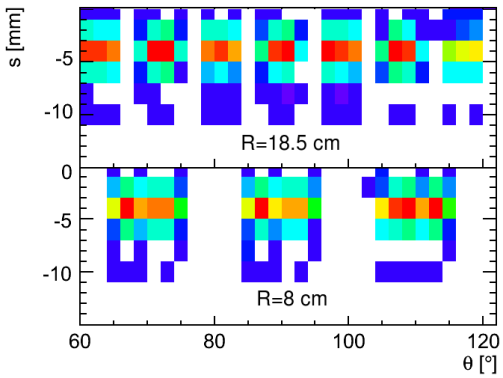

Figure 6.11: Part of the filtered sinogram for R=8 cm and R=18.5 cm. The smaller radius has bigger acceptance gaps due to the worse angular coverage.

Chapter 7

Conclusion and outlook

This thesis is devoted to the characterization of the PET test device featuring Multi Pixel Photon Counter readout. A MPPC is a new type of photon-counting device made of multiple avalanche photodiode pixels operated in Geiger mode [3]. The prototype consists of eight 2×2 MPPC arrays. Each 3600 pixel MPPC with a sensitive surface of $3 \times 3\,mm^2$ is coupled to one $15\,mm$ long LFS crystal of identical size. Each MPPC has been analyzed in terms of gain dependence on voltage and temperature. The expected linear dependence from gain and bias voltage have been confirmed. The breakdown voltage and pixel capacitance for each MPPC have been extracted from this measurement. Their small spread from channel-to-channel with an RMS less than 2% shows the uniformity of the MPPCs. The homogeneity of gain and breakdown voltage of all MPPCs in particular is a big advantage for PET devices with a large amount of channels and would make the development of readout electronics less difficult. Therefore, MPPCs have proven to be well suited for application in multi-channel systems.

The time constant has been calculated from the positive bias region of the IV-curve and the gain measurement. This result is in good agreement with the time constant extracted from an exponential fit on the waveform considering that both results have been derived from three independent measurements. The spread of parameter values extracted with either measurement is about 10 % RMS. This leads to the conclusion that the IV-curve and gain measurement are reliable characterization techniques.

The energy resolution has been investigated concerning voltage over breakdown and the integration range, as well as the dependency on the front end electronics. Measurements have shown that the energy resolution improves for higher voltages over breakdown and small integration range, to a point where too much noise is contributed by the voltage over breakdown and the integration range does not cover the primary part of the waveform any longer. The best energy resolution of $(14.7 \pm 1.6)\,\%$ has been achieved for an voltage of breakdown of $2.1\,V$ and an integration range of $220\,ns$. A comparison of two waveform analysis techniques (ADCM and QDC) has shown that integrating waveforms with a QDC improves the energy resolution by 1.9 % points on average. The ADCM is equipped with a fast and easy to handle DAQ program, suitable for the study of test devices, especially for multi-channel systems. However, for PET applications, where a good energy resolution is required, the QDC has shown a better performance than the ADCM.

With the gain measurement knowledge, each channel can be operate for a certain gain or voltage over breakdown. Thus, the mean of the photoelectric peak can be calculated from charge to number of fired pixel. Applying corrections for crosstalk and afterpulse, the number of detected photons can be calculated, which increases with voltage over breakdown due to the increase of the photon detection efficiency for higher voltages over breakdown. The channel-to-channel variation has a RMS of 14.3 % on a mean value of about 1200 detected photons.

The deviations between the channels arise primarily due to different crystal sizes and coupling between crystal and MPPC. Further optimization studies could decrease the spread of number of detected photons. Channels with particularly low number of detected photons could be investigated more precisely concerning crystal size and coupling to the MPPC. Since a high number of detected photons improves the time and energy resolution, this is an important task for future studies.

Both HV modules are calibrated and the bias voltage can be applied for each MPPC individually, with an accuracy of $36.3\,mV/ADU$. The module is also equipped with a temperature sensor for continuous temperature readout during a measurement. The slope of the linear correlation between breakdown voltage and temperature have been determined to $(55.95 \pm 0.4)\,mV/^{\circ}C$ which is consistent with the value quoted by Hamamatsu [3]. This correlation is then used to adjust the bias voltage with the HV module for temperature changes to keep the voltage over breakdown constant. This also leads to a constant crosstalk and afterpulse probability. Long term stability concerning the position of the photoelectric peak have been achieved within a range of $20\,pC$, which is due to the limited accuracy of the HV module.

The MPPC working point can be operated for two different read out options by adjusting the voltage with the HV module for all channels to the same mean of the photoelectric peak (method 1), or to the same gain (method 2). Method 1 has the advantage of a common Compton threshold, which can be applied during the measurement to reduce the amount of data. Method 2 equalizes the gain and, given the small spread in signal shape among the MPPCs, also the amplitude of one fired pixel. Therefore, the same threshold at 0.5 photoelectrons can be applied to each channel to trigger on the first photon detected, which is an essential feature for time resolution measurements. In previous studies, a coincidence time resolution of $350\,ps$ has been achieved [36]. It is foreseen to improve the PET test device by the time-of-flight information and extend it to a TOF PET device. For time resolution studies on multi-channel systems, the TOF PET can serve as a test bench for multi-channel read-out electronics with high timing performance.

Method 1 has been used for spatial resolution studies. For this purpose, a compound of two ^{22}Na sources with a distance of $10\,mm$ have been positioned in the center of the PET test device. At a detector radius of $11\,cm$, a scan has been performed which covers the surface ring to 83.4 % resulting in a total rate of the scan of $CR = 5.7\,kcps$, which is in good agreement with the theoretical expected rate calculated from the source activity. The image of the two source points have been reconstructed using the top part of both detector modules. The reconstructed image have been derived from a filtered backprojection applying a ramp filter which reduces the blurring of a simple backprojection significantly. From the x and y-projections on the image, the distance has been determined to $9.85\,mm$, which deviates by 1 % from the expected value. Five scans for different detector radii between $8\,cm$ and $18.5\,cm$ have been performed. The spatial resolution has been determined from a Gaussian fit on the x and y-projections of the corresponding images. No correlation between spatial resolution and detector radius have been observed. The mean spatial resolution of all scans is of the order of $(2.2 \pm 0.2)\,mm$. Theoretically, the spatial resolution should worsen by $0.2\,mm$ due to non-collinearity, but the acceptance of the detector also improves due to a better angular coverage of the field of view. Both effects have a small impact with respect to the precision of the measurement or cancel each other leaving the spatial resolution constant in all tested configurations. It is foreseen to extend the image reconstruction by the bottom layer of both detector modules in order to reconstruct 3D images. Furthermore, the spatial resolution will be investigated for different distances of the source to the center.

Bibliography

[1] J. S. Karp, S. Suleman Surti, M. E. Daube-Witherspoon, G. Muehllehner, "Benefit of Time-of-Flight in PET: Experimental and Clinical Results." *J Nucl Med*, vol. 49, no. 3, pp. 462-470, March 2008.

[2] S. Surti, A. Kuhn , M.E. Werner,A.E.Perkins, J.Kolthammer, J.S.Karp, "Performance of Philips Gemini TF PET/CT scanner with special consideration of its time of flight imaging capabilities." *J Nucl Med, vol. 48, pp. 471-480, March 2007*

[3] Hammamatsu Photonics,MPPC devices - Data sheet. [Onlin]. Available:www.hammamatsu.com

[4] Francesca Attanasi et al.,"Characterization of an In-Beam PET Prototype for Proton Therapy With Different Target Compositions." *IEE, vol. 57, No.3*, June 2010

[5] A.Braem et al.,"AX-PET: A novel PET detector concept with full 3D reconstruction." *NIM A ,* May 2009

[6] C.L. Kim, G.C. Wang, "Multi-Pixel Photon Counters for TOF-PET Detector and its challenges", *Nuclear Science Symposium Conference Record*, 2008.

[7] M. Göttlich, E. Garutti et al., "Application of Multi-Pixel Photon Counter to Positron Emission Tomography", *Nuclear Science Symposium Conference Report 2008, NSS '08 IEEE*, October 2008, Pages: 3119-3122

[8] END TOFPET-US & Ultrasound project , https://endotofpet-us.web.cern.ch

[9] J. Langner, "Development of a Parallel Computing Optimized Head Movement Correction Method in Positron Emission Tomography", University of Applied Sciences Dresden and Research Center Dresden-Rossendorf, 2003. Available: http://www.jens-langner.de/ftp/MScThesis.pdf

[10] Paul Suetens, "Fundamentals of Medical Imaging",*Cambridge University Press* , 2009,

[11] P. E. Valk, D. L. Bailey, D. W. Townsend, and M. N. Maisey, "Positron Emission Tomography: basic science and clinical practice", *Springer Verlag*, 2003

[12] Alexander Tadday, "Characterisation studies of Silicon Photomultipliers", Universität Heidelberg, 2008

[13] W.W. Moses, "Advantages of improved timing accuracy in PET cameras using LSOscintillator", *IEEE Transactions on Nuclear Science*, 3:1670-1675, November 2002

[14] A. Asano, "Computed Tomography - Image reconstruction from projections", Pattern Information Processing, 2009, Available: http://laskin.mis.hiroshima-u.ac.jp/kougi/07a/PIP/

[15] S.A. Jackson "Theory of Tomography", retrieved from radiology-physics.bitica.com, 2005

[16] L.Auvarez-Gaume et al., "Review of particle physics",physics letters B, pp.286-288, July 2008

[17] Joanna S. Salacka, Minesh K. Bacrania, "A Comprehensive Technique for Determining the Intrinsic Light Yield of Scintillators", *IEEE Trans Nucl Scence*, 57:901-909, 2010

[18] Harold Rothfussa, Larry Byarsb et. al, "Energy resolution and absolute detection efficiency for LSO crystals: A comparison between Monte Carlo simulation and experimental data", Siemens Medical Solutions, 2007

[19] S. Bowden and C. Honsberg, "Optical properties of silicon", Available: http://www.udel.edu/igert/pvcdrom/index.html

[20] Kwok K. Ng., "Complete guide to semiconductor devices", 2002

[21] N. Wattimena, "The calice tile hadron calorimeter prototype with silicon photomultiplier readout", *10th ICATPP converence on Astroparticle, Space physics, detectors and medical physics applications*, 2007

[22] P.Puzhan, B.Dolgoshein et. al, "An advanced study of silicon photomultiplier", *ICFA Instrum.Bull., 2001*

[23] Brian F. Aull, Andrew H. Loomis et al., "Geiger-mode avalanche photodiodes for three-dimensional imaging", *Lincoln Laboratory Journal*, 2002

[24] P.Eckert, H. Schultz-Coulon, W. Shen, R. Stamen, A. Tadday, "Characterisation Studies of Silicon Photomultipliers", Kirchhoff-Institut fuer Physik, Universitaet Heidelberg, arXiv:1003.6071v2 [physics.ins-det], 2009

[25] Zecotek, LFS Scintillation Material - Product Information. Available: www.zecotek.com

[26] S. Seifert et al., "Accurate Measurements of the Rise and Decay Times of Fast Scintillators with Solid State Photon Counters", in *Nuclear Science Symposium Conference Record* , 2010.

[27] E. Auffray, Cern, personal contact

[28] P. Buzhan, B. Dolgoshein et al."An advanced study of Silicon photomultiplier", Volkov Moscow Engineering and Physics Institute, Moscow et al., ICFA Instrumentation Bulletin, 2001

[29] HVSys, "HV cell for Silicon Detectors", Data sheet, Available: www.hvsys.dubna.ru

[30] ADCM, "ADCM-16", AFI Electronics, Available: http://afi.jinr.ru/ADCM-16HV

[31] QDC Lecroy 1182, Data sheet, Available: http://www.lecroy.com/lrs/dsheets/1182.html

[32] Na-22 decay scheme, University Waterloo, Available: http://www.safetyoffice.uwaterloo.ca/hse/radiation/rad_sealed/ decay/types/beta_plus.htm

[33] Keihley voltage supply, Available: http://ceot.ualg.pt/OptoEl/Datasheets/6487_901_01A.p

[34] Roman Greim, "SIPM arrays", RWTH Aachen University, talk at DPG-Frühjahrstagung, 2009

[35] "Yiping Shao, "A new timing model for calculating the intrinsic timing resolution of a scintillator detector", Dep. of Nuclear Medicine, State University New York, January 2007

[36] E.Auffray, Erika Garutti et al., "Towards a time-of-flight positron emission tomography system based on Multi-Pixel Photon Counter read-out ", *Nuclear Science Symposium Conference Report IEEE ,* 2010

[37] Martin Janecek, William W. Moses, "Optical Reflectance Measurements for Commonly Used Reflectors", *Nuclear Science EEE*, 2008

[38] S. Tavernier, "Positron Emission Tomography: Present Status and future prospects", Vrije Universiteit Brussel, NDIP Lyon, July 2011

[39] Hoffman EJ, Huang SC et al., "Quantitation in positron emission computed tomography: 6. Effect of nonuniform resolution" *J.Comput. Assist. Tomogr., 1982*

Danksagungen

Ich würde mein Diplom heute nicht in den Händen halten, wenn es nicht viele Menschen um mich herum gäbe, die mich immer unterstützt haben. Daher möchte ich mein Diplom zum Anlass nehmen um mich bei diesen Leuten zu bedanken. Anfangen möchte ich bei Dr. Erika Garutti, die mich während der Anfertigung meiner Diplomarbeit begleitet und mich mit zahlreichen Tipps und Anregungen und noch mehr Geduld unterstützt hat und bei Prof. Dr. Peter Schleper für seine Bereitschaft, meine Diplomarbeit als Zweitgutachter zu beurteilen. Mein Dank geht auch an Dr. Martin Goettlich, Dr. Alessandro Silenzi und Chen Xu, die sich immer Zeit für mich genommen haben, wenn ich Fragen und Probleme hatte. Sehr bedanken möchte ich mich an dieser Stelle bei Johannes Haase, der mich durch das gesamte Studium begleitet hat und ohne den ich die letzten 5 Jahre niemals diese Arbeit hätte schreiben können. Seine Freundschaft ausserhalb der Physik hat mich sehr geprägt. In diesem Zusammenhang möchte ich mich bei Niklas Hegemann bedanken, mit dem ich die Diplomarbeit zusammen geschrieben habe und der mir in schwierigen Zeiten immer zur Seite stand. Zum Schluß möchte ich mich ganz herzlich bei meiner Familie bedanken. Meine Eltern wollten immer das Beste für mich und haben mich in jedem Lebensabschnitt untersützt ohne mich je unter Druck zu setzen. Großer Dank geht ebenfalls an meine zwei Brüder, die immer für mich da waren und für die ich sehr dankbar bin.

Selbständigkeitserklärung

Hiermit erkläre ich, dass ich die vorgelegte Diplomarbeit eigenhändig, ohne unerlaubte fremde Hilfe und unter Zuhilfenahme der angegebenen Quellen verfasst habe.